Sutar and Jadhav *Biochar (2025)7:11*
https://doi.org/10.1007/s42773-024-00406-2

Biochar

ORIGINAL RESEARCH Open Access

"Theory of Pore Conflation" and "Shubhjyot's equation" in the treatment of Brilliant green dye-contaminated water using Jamun leaves biochar

Shubham Sutar[1] and Jyoti Jadhav[1*]

Abstract

This study investigates the adsorption of Brilliant Green (BG) dye onto biochar derived from *Syzygium cumini* (Jamun) leaves (JLB). Biochar was produced via pyrolysis at 800 °C and examined employing various methods, including Scanning electron microscopy (SEM–EDX), Fourier transform infrared spectroscopy (FTIR), X-ray diffraction (XRD), Brunauer–Emmett–Teller (BET) analysis, Raman spectroscopy, Zeta potential and X-ray photoelectron spectroscopy (XPS). The optimum parameters for BG dye adsorption, determined by batch adsorption studies, were a temperature of 80 °C, an initial dye concentration of 500 mg L^{-1}, a contact period of 30 min, and an agitation speed of 400 RPM. The maximum adsorption capacity of JLB for BG was 243.90 mg g^{-1}. It was found that the adsorption process adhered to the Freundlich isotherm model and pseudo-second-order kinetics, revealing heterogeneous adsorption with chemisorption. A novel "Theory of Pore Conflation" was proposed to explain enhanced adsorption at higher temperatures, supported by SEM and FTIR analyses. Additionally, a new equation termed "Shubhjyot's equation" was introduced to account for time dependency in adsorption capacity calculations. The thermodynamic analysis demonstrated that the process is endothermic and spontaneous. Isopropanol was the most effective organic solvent for desorption studies, demonstrating biochar regeneration potential for up to five cycles. Phytotoxicity and cyto-genotoxicity assessments demonstrated the environmental safety of JLB compared to BG dye. The use of JLB production offers a way to repurpose agricultural waste, contributing to circular economy principles. This extensive study demonstrates JLB's promise as an effective, economical, and environmentally safe adsorbent for wastewater treatment that eliminates textile dyes.

Highlights

- JLB demonstrated high q_e (243.90 mg g^{-1}) for BG dye removal from water.
- Optimal adsorption conditions were identified: 80 °C temperature, 500 mg L^{-1} initial dye concentration, 30 min contact time, 400 RPM agitation speed.
- A novel "Theory of Pore Conflation" was proposed to explain enhanced adsorption at high temperatures due to the merging of adjacent pores.
- "Shubhjyot's equation" was introduced to model time-dependent transient adsorption capacity.
- JLB showed good reusability over 5 adsorption–desorption cycles using isopropanol as eluent.
- Phytotoxicity and cytotoxicity studies confirmed JLB is environmentally safe compared to the BG dye.

*Correspondence:
Jyoti Jadhav
jpj_biochem@unishivaji.ac.in

Keywords Theory of Pore Conflation, Shubhjyot's equation, Adsorption, Biochar, Brilliant green, Kinetics

Graphical Abstract

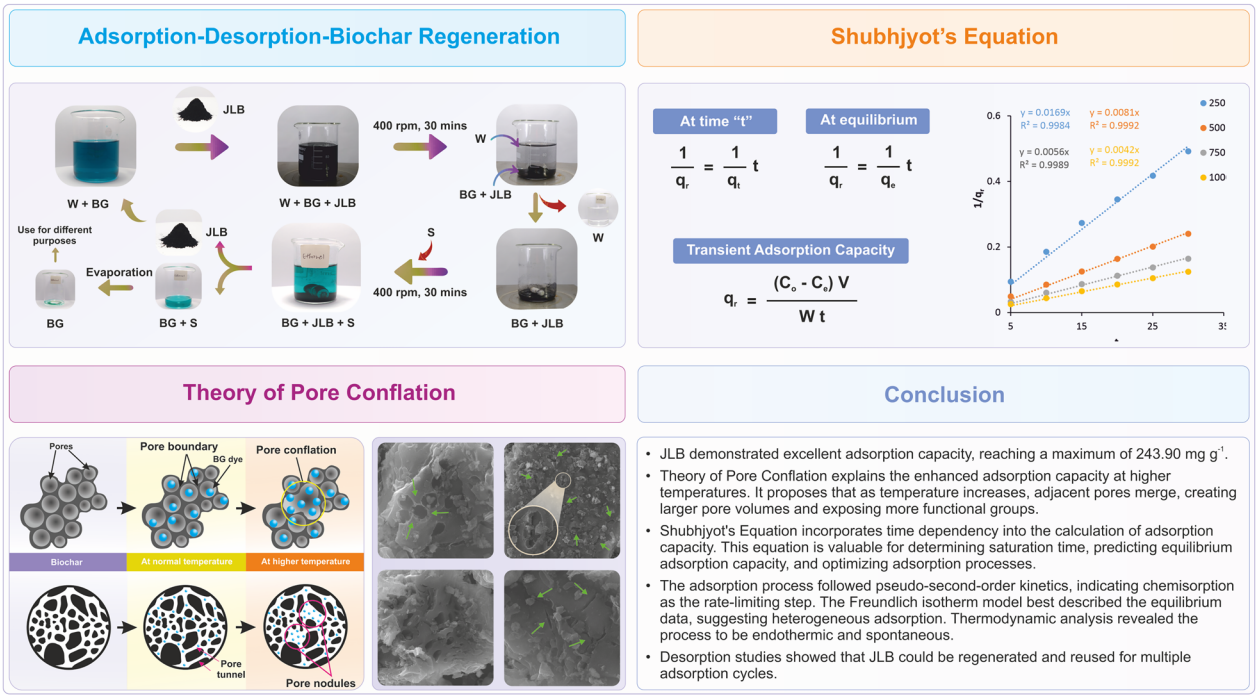

1 Introduction

Adsorption is the peculiarity of specific living and non-living substances to adsorb the solute molecules from aqueous system. In recent years, lignocellulosic waste generated from agriculture has been used extensively to construct biochar for the adsorption of hazardous materials such as dyes, heavy metals, pesticides, and pharmaceutical waste (Goswami et al. 2022). These synthesized biochar materials are highly porous and have great affinity towards adsorbate due to the presence of different functional groups (Jabar et al. 2023). Brilliant green (BG) belongs to the triaryl methane dye category, having a complex aromatic structure. It is highly soluble in water. Its antibacterial, ectoparasitic, and fungicidal activities have been reported. Owing to this, people have been exploiting it to treat infections in aquaculture industries and fisheries and as a therapeutic agent in the medical field. Different industries, such as paper, toys, plastic, leather, dyeing silk, and cotton, have been utilizing it as a coloring agent due to its stable and recalcitrant nature (Sahu et al. 2020). Its carcinogenic, mutagenic, and teratogenic properties have been noted due to the fact that US FDA has prohibited its use. The release of such dye-contaminated wastewater from different industries causes environmental pollution. It is, therefore, important to adsorb BG from the effluent before its dismissal into the environment (Belcaid et al. 2023).

Different adsorbent materials have been implemented to treat dye-contaminated wastewater. Traditional approaches to eliminating dyes include coagulation-flocculation (Nnaji et al. 2022), chemical oxidation (Fatimah et al. 2024), membrane separation process (Pervez et al. 2024), electrochemical (Lei et al. 2024), aerobic, and anaerobic microbial degradation techniques (Monga et al. 2022). These approaches are significantly accessible and used globally, but they have not been found to be efficient because they are costly, less environment-friendly and laborious to perform (Bushra et al. 2021). Secondary metabolites produced as a result of microbial breakdown pose a threat to the environment. Membrane filtration requires a lot of energy, is costly, and can foul easily (Pervez et al. 2024).

Biosorption is a process that uses biomass to remove pollutants from water. Biosorbents, comprising fungi,

bacteria, polysaccharide sorbents, and algae, are economically viable and readily accessible, with their effectiveness dependent upon the dye type and experimental variables such as initial dye concentration, pH, temperature, and contact period. Therefore, biosorbents with improved dye adsorption capacity are favored (Praveen et al. 2022). Biosorbents derived from microbes and polysaccharides may exhibit enhanced selectivity in their adsorption properties (Wang et al. 2022). More specialized production procedures are potentially needed for biosorbents based on microorganisms and polysaccharides (Dawwam et al. 2023; Blaga et al. 2021). Microbial and polysaccharide-based biosorbents have varying capacities for regeneration, but they are often not as strong as biochar. In contrast, the high flexibility of biochar allows it to effectively absorb a wide range of contaminants, such as organic pollutants and heavy metals. Biochar can be generated from various waste products, rendering it potentially more economical and sustainable. Various adsorbents, including activated carbon, metal oxide-based materials, carbon-based materials, metal–organic frameworks (MOFs), and polymer-based materials, are widely employed for dye adsorption from polluted water (Dutta et al. 2021). These adsorbents provide advantages including ease of manufacture, significant effective surface area, multifunctionality, increased surface volume ratio, strong reactivity, abundant active sites, recyclability, low cost, and high efficiency in treating recalcitrant materials (Godiya et al. 2020). In recent years, there has been a decrease in the use of traditional absorbents, such as activated carbon, silica, clay, etc., due to different reasons (Li et al. 2023a, b). Activated carbon, although effective, can be expensive to produce and regenerate. For example, commercial activated carbons can cost $500–1500 per ton, while biochar costs only $50–200 per ton (Ambaye et al. 2021). Silica and clay materials often have lower adsorption capacities compared to biochar. A study comparing rice husk biochar to commercial silica found that biochar had over 3 times higher adsorption capacity for methylene blue dye (Viotti et al. 2024). Biochar has demonstrated high adsorption capacities for various contaminants. For instance, in this work, the maximum adsorption capacity of jamun leaves biochar for brilliant green dye is 243.90 mg g^{-1}. Other biochar materials such as areca nut (*Areca catechu L.*) husk biochar with 105.43 mg g^{-1} (Tharayil and Chinnaiyan 2023), soybean residue (okara) biochar with 19.30 mg g^{-1} (Shan et al. 2022), date palm petioles biochar with 123.38 mg g^{-1} (Aichour et al. 2022), Doum palm (*Hyphaene thebaica*) shells biochar with 117.92 mg g^{-1} (Tcheka et al. 2024) and *Manihot esculenta* stalk with 22.30 mg g^{-1} (Gajendiran et al. 2024). These findings highlight the varying effectiveness of different biochar materials in contaminant removal, with jamun leaves emerging as particularly efficient among the materials studied. This compares favorably to activated carbon (90–400 mg g^{-1}) (Kosale et al. 2023), clay (65–160 mg g^{-1}) (Satyam and Patra 2024), and some MOFs (50–300 mg g^{-1}) (Isaeva et al. 2021). However, certain nanomaterials like graphene oxide can achieve even higher capacities (> 1000 mg g^{-1}) (Infurna et al. 2023). Biochar can often be regenerated through simple washing with solvents or thermal treatment (Amdeha 2023). This gives it an advantage over clay, which has limited regeneration potential. Activated carbon requires energy-intensive thermal or chemical regeneration (Bhandari et al. 2023). MOFs and nanomaterials can be regenerated but may lose capacity over multiple cycles (Muoghalu et al. 2023). Compared to other biochar precursors, jamun leaves are abundantly available as agricultural waste in many tropical and subtropical regions. This makes it a very low-cost and sustainable feedstock. The leaves also have a high carbon content and low ash content, which leads to biochar with favorable adsorption properties (Wang et al. 2024; Li et al. 2023a, b). Nowadays, biochar manufactured from agriculture and related industrial waste has got researcher's attention due to their high adsorption capacity (typically 100–500 mg g^{-1}), mesoporous nature, regeneration efficiency (80–90% capacity retention after 5–10 cycles), low operation cost ($50–200 ton^{-1}), stability, and spontaneity of reaction. Also, pyrolysis in the limited oxygen environment is an alternative method for traditional adsorbents in terms of cost (Subratti et al. 2021). Biochar leaches less hazardous chemicals into treated water than other synthetic adsorbents, cleaning the effluent. Biochar adsorption does not produce poisonous byproducts like certain chemical treatments.

This research paper delves into the realm of dye adsorption using biochar, specifically focusing on the adsorption of the triaryl methane dye Brilliant Green (BG). The research utilizes biochar synthesized from *Syzygium cumini* leaves as a cost-effective and eco-friendly precursor for BG dye adsorption. Jamun trees (*Syzygium cumini*) are widely grown in many tropical and subtropical regions. The leaves are often abundant and available as agricultural or garden waste. This investigation includes a comprehensive surface characterization of the synthesized biochar (UV–visible, SEM–EDX, FT-IR, XRD, Zeta potential, Raman, BET and XPS), analysis of kinetic, isotherm, and thermodynamic data. The paper identifies an unexplored mechanism related to temperature dependency during the adsorption process, termed the "Theory of Pore Conflation". It also introduces a modification to the traditional equation for adsorption capacity, now accounting for time dependency, referred to as "Shubhjyot's equation". Additionally, an investigation into

toxicity assessment using phytotoxicity and cyto-genotoxicity assessments was conducted.

2 Materials and methods

2.1 Preparation of biochar

The JLB preparation illustration is shown in Fig. S1. The dirt particles were first removed from the *Syzygium cumini* leaves through cleansing. A mixer was then used to smash the material into a fine powder. After that, the powder was passed through a mesh sieve with a 1 mm opening. In low oxygen environments (800 °C for 20 min), biochar was generated in a muffle furnace (ADITI ASSOCIATE, India). In the end, the biochar was sequentially washed in hot, chilled, and room temperature water for 5 h on a magnetic stirrer at a speed of 300 RPM (Revolutions per minute). The biochar was subsequently dried in an oven maintained at 50 °C. Following the drying, the biochar was crushed into a fine powder using a mortar and pestle for further evaluation.

2.2 Characterization

JLB's specific surface area, total pore volume, and mean pore diameter were analyzed using BET (Brunauer–Emmett–Teller) analysis (Quantachrome NovaWin, Quantachrome Instruments v11.02). SEM (Scanning electron microscope) examination was conducted using a JSM-IT200 SEM from JEOL USA. A Fourier-infrared spectrometer was utilized to analyze the functional groups present on the surface of JLB (FTIR-7600, Lambda Scientific Pty Ltd., Australia). The Sigma-Aldrich IR Spectrum Table & Chart (https://www.sigmaaldrich.com/IN/en/technical-documents/technical-article/analytical-chemistry/photometry-and-reflectometry/ir-spectrum-table) was used to characterize functional groups. A Renishaw micro-Raman inVia spectrometer was utilized for the Raman analysis. The surface charge of the JLB was determined using Zeta potential, Nano ZS90, Malvern, UK. An analysis of XRD (X-ray diffraction analysis) was performed utilizing a D2 Phaser model from Bruker Ltd. Germany. X-ray photoelectron spectroscopy (XPS) was assessed using a JEOL Japan (Model: JPS-9030).

2.3 Batch adsorption studies.

The influence of temperature on JLB-BG interaction was studied by keeping experimental parameters as T = 20, 40, 60 and 80 °C, BG = 250 mg L^{-1}, JLB = 0.2 g, RPM = 600, t = 30 min, V = 0.05 L, and pH = 7. The impact of contact time on the adsorption process was studied by analyzing the samples at time intervals of 0–30 min, BG = 250 mg L^{-1}, JLB = 0.2 g, RPM = 600, T = 80 °C, V = 0.05 L, and pH = 7. The impact of RPM on the adsorption process was studied by analyzing the samples at 100–400 RPM, BG = 250 mg L^{-1}, JLB = 0.2 g, T = 80 °C, V = 0.05 L, and pH = 7. The initial decolorization assay was executed by varying concentrations of BG from 500–2000 mg L^{-1}, JLB = 0.2 g, T = 80 °C, t = 30 min, RPM = 600, V = 0.05 L and pH = 7. The amount of BG adsorbed by JLB at time t (min), q_t (mg g^{-1}), q_e (mg $g.^{-1}$) at equilibrium, and % R was calculated using the following relations (Kim et al. 2023)

$$q_e = C_o - C_e \frac{V}{W} \quad (1)$$

$$q_t = C_o - C_t \frac{V}{W} \quad (2)$$

$$R\,(\%) = \frac{C_o - C_e}{C_o} \times 100 \quad (3)$$

where C_o, C_e, and C_t (mg L^{-1}) are the initial, equilibrium, and at a time concentrations of BG, respectively. V (L) is the volume of solution, W (g) is the weight of JLB used, and R is the removal efficiency (%).

2.4 Kinetics

The kinetic study was executed by varying the initial concentration of BG at 250–1000 mg L^{-1}. The other experimental parameters were set as JLB = 0.2 g, T = 80 °C, t = 30 min, RPM = 600, V = 0.05 L and pH = 7. The rate of adsorption by JLB was monitored at time intervals of five minutes until equilibrium. The kinetic data obtained were assessed using four commonly used kinetic models viz., pseudo-first order (PFO), pseudo-second order (PSO), intraparticle diffusion (IPD) and liquid film diffusion (LFD).

The PFO reaction model is frequently employed to characterize dye adsorption kinetics on biochar. It posits that the adsorption rate is directly connected to the number of vacant pores on the biochar surface (Aljeboree et al. 2017). The PFO model is generally used for pure physical adsorption, where the adsorption rate is directly proportional to the amount of solute present. It posits that the rate-limiting step is film diffusion and is unaffected by the concentrations of the reactants (physisorption) (Li 2019). The PFO kinetic equation is presented as follows:

$$\ln(q_e - q_t) = \ln(q_e) - \left(\frac{k_1}{2.303}\right) t \quad (4)$$

where k_1 (min^{-1}) represents the rate constant for PFO kinetic model. q_e and q_t (mg g^{-1}) are the adsorption capacities at equilibrium and time "t". The value of k_1 was measured from the plot of log (q_e-q_t) vs. t.

The PSO model posits that adsorption capacity is directly proportional to the number of active sites occupied on the adsorbent surface (Singh et al. 2022).

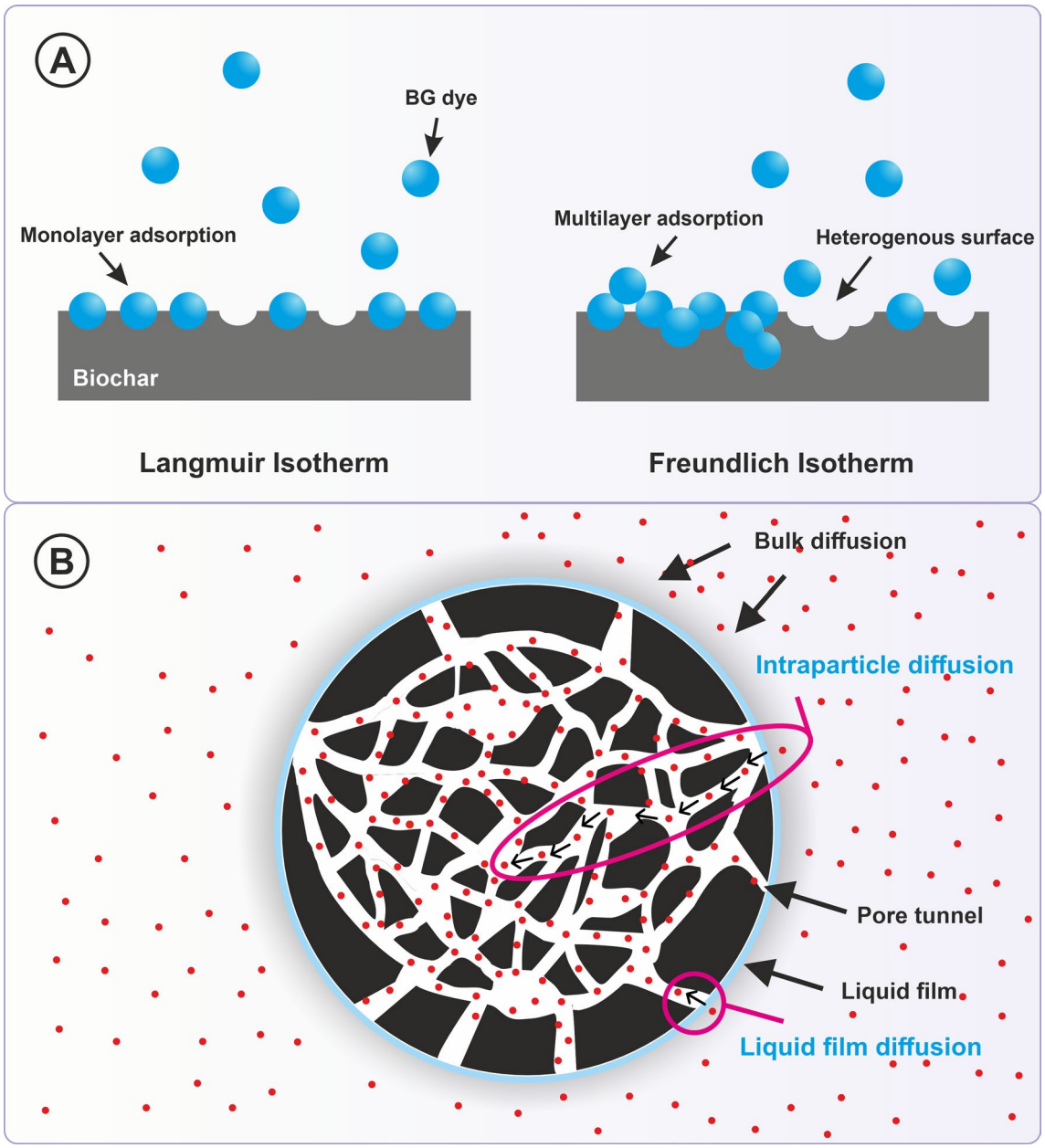

Fig. 1 Illustrations for the kinetics of dye adsorption **A** Langmuir and Freundlich isotherm and **B** intraparticle and liquid film diffusion (Sutar et al. 2022)

The PSO model posits that the rate-limiting stage in adsorption is chemisorption, characterized by valence forces resulting from the sharing or exchange of electrons between the adsorbent and contaminant (Praveen et al. 2022). The following is an expression for the PSO kinetic equation:

$$\frac{t}{q_t} = \left(\frac{1}{k_2 q_e^2}\right) + \left(\frac{1}{q_e}\right) t \quad (5)$$

k_2 (g mg^{-1} min^{-1}) is the PSO rate constant. The value of k_2 was calculated from the linear plot of t/q_t vs t. q_e and q_t (mg g^{-1}) are the adsorption capacities at equilibrium and time "t". h (mg g^{-1} min^{-1}) is the initial adsorption rate, evaluated using the equation, $h = k_2 q_e^2$.

LFD assumes the transport of dye molecules via the liquid film developed around the biochar to access the exterior surface (Fig. 1B) (Chen et al. 2022). This mechanism often occurs during the initial phase of adsorption,

marked by rapid dye absorption. The thickness of the stationary liquid film (boundary layer) is essential in determining the rate of LFD. Increased boundary layer thickness leads to reduced diffusion rates (Ojedokun and Bello 2017). LFD frequently occurs parallel with additional mechanisms such as intraparticle diffusion. In most adsorption processes, a transition occurs from LFD control during the initial phases to intraparticle diffusion control as adsorption proceeds (Phuong et al. 2019). The linear mathematical representation of this model is as follows (Ramath et al. 2023).

$$\ln(1 - F) = -k_{fd}\, t + C_L \tag{6}$$

K_{fd} (min^{-1}) represents the rate constant for LFD, t (min) is time, and C_L is the rate constant associated with the boundary layer. F represents the fractional attainment of equilibrium, $F = q_t/q_e$. The values of K_{fd} and C_L were calculated from a linear plot of ln (1-F) vs. t.

IPD is a mass transfer process that occurs during the adsorption of dyes onto biochar. The process entails the diffusion of dye molecules into the internal pores of the biochar following the initial surface adsorption (Fig. 1B) (Phuong et al. 2019). It frequently represents the rate-limiting step of adsorption process, especially following the initial rapid adsorption phase. Higher initial dye concentrations typically result in stronger concentration gradients, providing a larger driving force for the IPD process (Oyekanmi et al. 2024). Typically, the IPD process consists of the following stages:

- Phase I: External diffusion, also known as LFD, is the process by which dye molecules are moved from the bulk liquid phase to the exterior surface of biochar.
- Phase II: Dyes diffuse into the pores of biochar through IPD, which occurs from outside (Aqueous solution). Usually, this stage moves more slowly than phase I.
- Phase III: IPD slows down due to low dye concentration and fewer accessible adsorption sites (Phuong et al. 2019).

Based on the above concept, IPD is not always the only step that controls the rate. The kinetic equation for IPD can be expressed as follows:

$$q_t = k_{id}\, t^{0.5} + C_i \tag{7}$$

k_{id} ($mg\ g^{-1}\ min^{-0.5}$) represents the IPD rate constant, $t^{0.5}$ ($min^{0.5}$) is the square root of the time, and C_i reflects the boundary layer thickness. q_t ($mg\ g^{-1}$) is the adsorption capacity at a time "t." The values of k_{id} and C_i were evaluated from the plot of q_t against $t^{0.5}$.

2.5 Isotherm

Adsorption isotherm experiments were performed at different temperatures, such as 30, 50, and 70 °C. However, the initial concentrations of BG varied from 500 to 2000 mg L^{-1}. The rest of the parameters were kept as JLB = 0.2 g, t = 30 min, RPM = 600, V = 0.05 L, and pH = 7. The equilibrium data obtained was evaluated using four commonly used isotherm models viz., Freunlich (Eq. 8), Langmuir (Eq. 9), D-R (Eq. 10), and Temkin (Eq. 11).

The Langmuir isotherm assumes monolayer adsorption on an even surface with a limited quantity of equivalent adsorption sites (Fig. 1A). The model implies an equivalent adsorption energy over the biochar surface for adsorption (Abdu et al. 2024). The adsorption process is both reversible and dynamic, characterized by proportional rates of adsorption and desorption at equilibrium. The linearized mathematical equation of this model is presented as follows:

$$\frac{C_e}{q_e} = \frac{1}{kb} + \frac{C_e}{b} \tag{8}$$

Langmuir adsorption capacity is expressed as b ($mg\ g^{-1}$), q_e ($mg\ g^{-1}$) is the adsorption capacity at equilibrium, C_e ($mg\ L^{-1}$) is the BG concentration at equilibrium, and the Langmuir binding constant is represented by k ($L\ mg^{-1}$).

The Freundlich isotherm (Fig. 1A) proposes the presence of heterogeneous adsorption sites on the biochar surface, characterized by varying adsorption energies. This leads to a heterogeneous adsorption distribution across the surface, with molecules preferentially adsorbing from the highest energy sites (Singh et al. 2022).

$$\ln(q_e) = \ln(K_f) + \frac{1}{n}\ln(C_e) \tag{9}$$

where K_f ($mg\ g^{-1}$) and n are, respectively, the Freundlich constant and the heterogeneity factor. q_e ($mg\ g^{-1}$) is the adsorption capacity and C_e ($mg\ L^{-1}$) is the BG concentration at equilibrium.

The D-R (Dubinin-Radushkevich) model assumes a heterogeneous surface and aids in determining whether the adsorption process is physical or chemical (Batool et al. 2023). This model proposes that adsorption proceeds via the filling of micropore volume instead of through layer-by-layer surface covering. The model includes the principle of adsorption potential, reflecting the variation in Gibbs free energy when an adsorbent captures a unit molar mass of adsorbate (Hu and Zhang 2019). The linearized mathematical equations of these models in the respective order are given below (Salah omer et al. 2022).

$$\ln(q_e) = \ln(q_{DR}) - \beta\varepsilon^2 \tag{10}$$

where q_{DR} (mg g^{-1}) is the maximum adsorption capacity, q_e (mg g^{-1}) is the adsorption capacity at equilibrium, and β (mol^2 J^{-2}) is the average free energy produced per gm of the adsorbent. The values of q_{DR} and β were calculated from the linear plot of ln q_e against ε^2. The value of β was then used to calculate the mean free energy of adsorption (E). ε is the Polanyi potential energy (J mol^{-1}).

The Temkin adsorption isotherm is a fundamental model used to describe the adsorption equilibrium between adsorbate molecules and a heterogeneous adsorbent surface. The Temkin isotherm makes two main assumptions (Zand and Abyaneh 2020):

- An even arrangement of heterogeneous binding sites exists on the adsorbent external surface.
- The binding energy displays a linear variation across these distinct binding sites.

$$q_e = \frac{RT}{b_T} \ln A_T + \frac{RT}{b_T} \ln C_e \quad (11)$$

A_T and B_T are constants, R is the universal gas constant (8.31 J mol^{-1} K^{-1}), q_e (mg g^{-1}) is the adsorption capacity at equilibrium, and C_e (mg L^{-1}) is the BG concentration at equilibrium. T is the temperature (K). The values of A_T and B_T were obtained from a linear plot of q_e against ln C_e.

2.6 Thermodynamics

The experimental set-up for the thermodynamics study was like those on the influence of temperature on the adsorption process, as elucidated earlier. The following equations were utilized to calculate the values of standard free energy (ΔG°), standard entropy (ΔS°), and standard enthalpy (ΔH°) allied with the adsorption of BG by the JLB (Wang et al. 2023).

$$\Delta G^0 = \Delta H^0 - T\Delta S^0 \quad (12)$$

$$K_d = \frac{q_e}{C_e} \quad (13)$$

$$\ln K_d = \frac{\Delta S^0}{R} - \frac{\Delta H^0}{RT} \quad (14)$$

The values of ΔH° and ΔS° were calculated from a linear plot of ln K_d vs T^{-1}. R (8.31 J mol^{-1} K^{-1}) is the gas constant, q_e (mg g^{-1}) is the adsorption capacity, K_d is the distribution coefficient, C_e (mg L^{-1}) is the BG concentration at equilibrium and T (Kelvin (K)) is the temperature.

2.7 Dye desorption.

The quantity of dye desorbed q_d (mg g^{-1}) by JLB and % desorption efficiency, D was calculated using the following equations (Park et al. 2019; Sterenzon et al. 2022).

$$q_d = C_d \frac{V}{W} \quad (15)$$

$$\%\, D = \frac{q_d}{q_e} \times 100 \quad (16)$$

where C_d (mg L^{-1}) is the final concentration of BG in the solvent, V (L) is the volume of solvent, W (g) is the weight of JLB, and q_e (mg g^{-1}) is the adsorption capacity.

2.8 Phyto-toxicity

Black peas (*Vigna radiata L.*) seeds were employed to evaluate the toxicity of JLB and BG. Ten seeds were sown in autoclaved silica-filled seedling trays containing 0.1 g L^{-1} BG dye and 0.2 g of JLB per gram of silica in the corresponding block of silica-filled seedling trays. The JLB was evenly distributed within the silica-infused blocks of the seedling tray. Seed germination in water with silica-infused blocks was evaluated as a control. The phytotoxicity examination was conducted at room temperature and a pH of 7.0 ± 0.2 for 15 days, during which the plants were irrigated with identical solutions. All trials were conducted in triplicate, and phytotoxicity parameters were assessed (Patil et al. 2020).

$$\%\, G = \frac{\text{Number of germinated seeds}}{\text{Total number of planted seeds}} \times 100 \quad (17)$$

$$\%\, I = \frac{(\text{Number of planted seeds} - \text{Number of germinated seeds})}{\text{Total number of planted seeds}} \times 100 \quad (18)$$

$$RLSTI = \frac{\text{Root length of stress plant}}{\text{Root length of control plant}} \times 100 \quad (19)$$

$$SLSTI = \frac{\text{Shoot length of stress plant}}{\text{Shoot length of control plant}} \times 100 \quad (20)$$

$$Chl\,a\,(mg\,g^{-1}) = [(12.7 \times A663) - (2.69 \times A645)] \times \frac{\text{Acetone (L)}}{\text{Leaf tissue (g)}} \times 100 \quad (21)$$

$$Chl\ b\ (mg\,g^{-1}) = [(22.9 \times A645) - (4.68 - A663)] \times \frac{\text{acetone (L)}}{\text{Leaf tissue (g)}} \times 100 \quad (22)$$

$$\text{Total Chl} = \text{Chl a} + \text{Chl b} \quad (23)$$

where Germination (G), Inhibition of germination (I), Root length stress tolerance index (RLSTI), Shoot length stress tolerance index (SLSTI), Chlorophyll (Chl), L for volume in liters, g for weight in grams, and A for absorbance.

2.9 Cyto-toxicity

The *Allium cepa* root tip assay was utilized to conduct cell cyto-genotoxicity investigation. The JLB concentration used was 0.2 g. The BG dye concentration utilized was 20 mg L^{-1}. The process of germination in water served as a control for this experiment. The experiment was conducted for 15 days at the appropriate doses, at room temperature, and with a pH of 7.0 ± 2. Daily restorations included dye solution and JLB with the same concentrations. After the exposure period was completed, the staining process was carried out, and the mitotic index and the percentage of abnormal cells were computed (Patil et al. 2020).

3 Result and discussion

3.1 Surface characterization

The SEM image (Fig. 2A) of JLB revealed a porous structure with a variety of particle sizes and shapes. The presence of small cavities, cracks, and a complex pore network system indicates that the JLB surface is heterogeneous (Aichour et al. 2022). The EDX elemental analysis (Fig. 2B and C) showed that the JLB is primarily composed of carbon (82.72%), oxygen (15.14%), and calcium (1.18%). The presence of calcium suggests some ash content, while the presence of oxygen indicates the existence of oxygen-containing functional groups (Ambaye et al. 2021). The presence of agglomerates is responsible for affecting the bulk density and flowability of the biochar. Table S1 depicts the various N_2 adsorption isotherm analysis variables. Large surface area of JLB (252.36 m^2 g^{-1}) helps with BG adsorption by providing more sites for dye molecules to bind. The total volume of pores (0.39 cc g^{-1}) within the JLB with a pore diameter of 2.82 nm suggests the mesoporous nature of JLB (Mansour et al. 2020). Zeta potential is an examination of the electrical charge on the surface of a particle in a liquid solution. It is a crucial characteristic that can have an impact on the interaction, aggregation, and stability of particles (Tokarčíková et al. 2023). The mean zeta potential of JLB, as indicated in Fig. 2D, was -14.8 mV; this negative value suggested that the JLB surface is negatively charged.

The FTIR spectrum (Fig. 3A) of biochar is a fingerprint that can be used to identify the functional groups present on the surface of the material. These functional groups play a vital role in the absorption of BG dye. The following are some of the key features of the FTIR spectrum that are relevant to the adsorption of BG dye:

1. 2879.6 cm^{-1}: This peak is often associated with the stretching vibrations of C–H bonds in aliphatic (saturated) hydrocarbons. It indicates the presence of methylene ($–CH_2–$) or methyl ($–CH_3$) groups (Liang et al. 2020).
2. 2394.3 cm^{-1}, 2341.2 cm^{-1}, and 2306.6 cm^{-1}: These peaks correspond to the presence of CO_2 or other gas impurities trapped in the JLB matrix, indicating the stretching vibrations of carbon dioxide.
3. 1582.6 cm^{-1}: This peak can be attributed to the C=C stretching vibrations in aromatic rings. It suggests the presence of aromatic compounds or graphitic structures within the JLB (Ray 2020).
4. 1435.7 cm^{-1}: This peak could be related to the bending vibrations of C–H bonds in aliphatic groups. It may also indicate the presence of aromatic C=C stretching vibrations or carboxylate ions (COO^-) (Tcheka et al. 2024).
5. 1038.1 cm^{-1}: This peak is typically assigned to the C–O stretching vibrations, suggesting the presence of alcohols, ethers, or carboxylic acids (Aichour et al. 2022).
6. 872.9 cm^{-1}: This peak is likely due to out-of-plane bending vibrations of C–H bonds in aromatic rings. It indicates the presence of substituted benzene rings.
7. 701.6 cm^{-1}, 656.7 cm^{-1}, and 599.6 cm^{-1}: These peaks may correspond to various bending vibrations associated with aromatic rings or other complex molecular structures within the biochar (Gajendiran et al. 2024).

In summary, the peaks for the hydroxyl groups, carbonyl groups, and aromatic rings were all very intense, which suggested that these functional groups were abundant in the JLB.

In the present study, XRD was employed to determine the structure of biochar, its crystallinity, and the extent of graphitization. The analysis (Fig. 3B) of JLB exhibited a mixed composition, containing both graphitic and non-graphitic carbon structures. The non-graphitic carbon may be the uncarbonized substance that remains after the pyrolysis process. 23° peak is often associated with graphitic carbon or disordered carbon structures. It suggests the presence of some graphitic domains within the biochar. 29° peak is commonly attributed to cellulose or other related organic compounds that might still be present in biochar (Liang et al. 2020). 35° peak indicates the presence of certain inorganic compounds, potentially clay minerals or silica. 39° peak, along with the peaks at 43°, 47°, and 48°, suggests the presence of crystalline phases, potentially calcium carbonate ($CaCO_3$) or other mineral compounds (Gale et al. 2021). This mixed composition underscored the heterogeneous nature of the JLB, with contributions from both carbonized and uncarbonized materials, as well as various inorganic

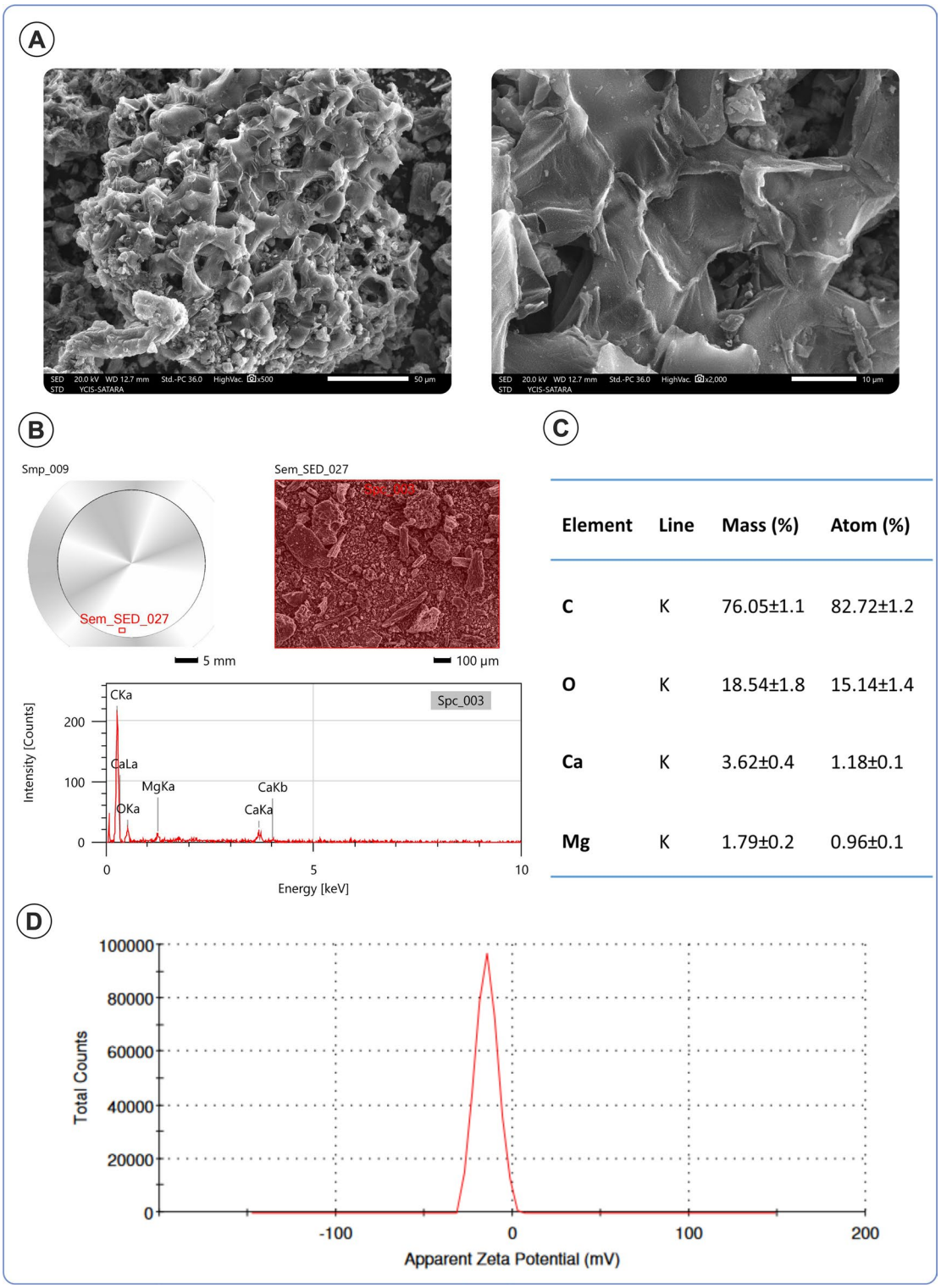

Element	Line	Mass (%)	Atom (%)
C	K	76.05±1.1	82.72±1.2
O	K	18.54±1.8	15.14±1.4
Ca	K	3.62±0.4	1.18±0.1
Mg	K	1.79±0.2	0.96±0.1

Fig. 2 SEM photographs (**A**) for JLB with EDX analysis graph (**B**) and table of elements (**C**), and zeta potential (**D**)

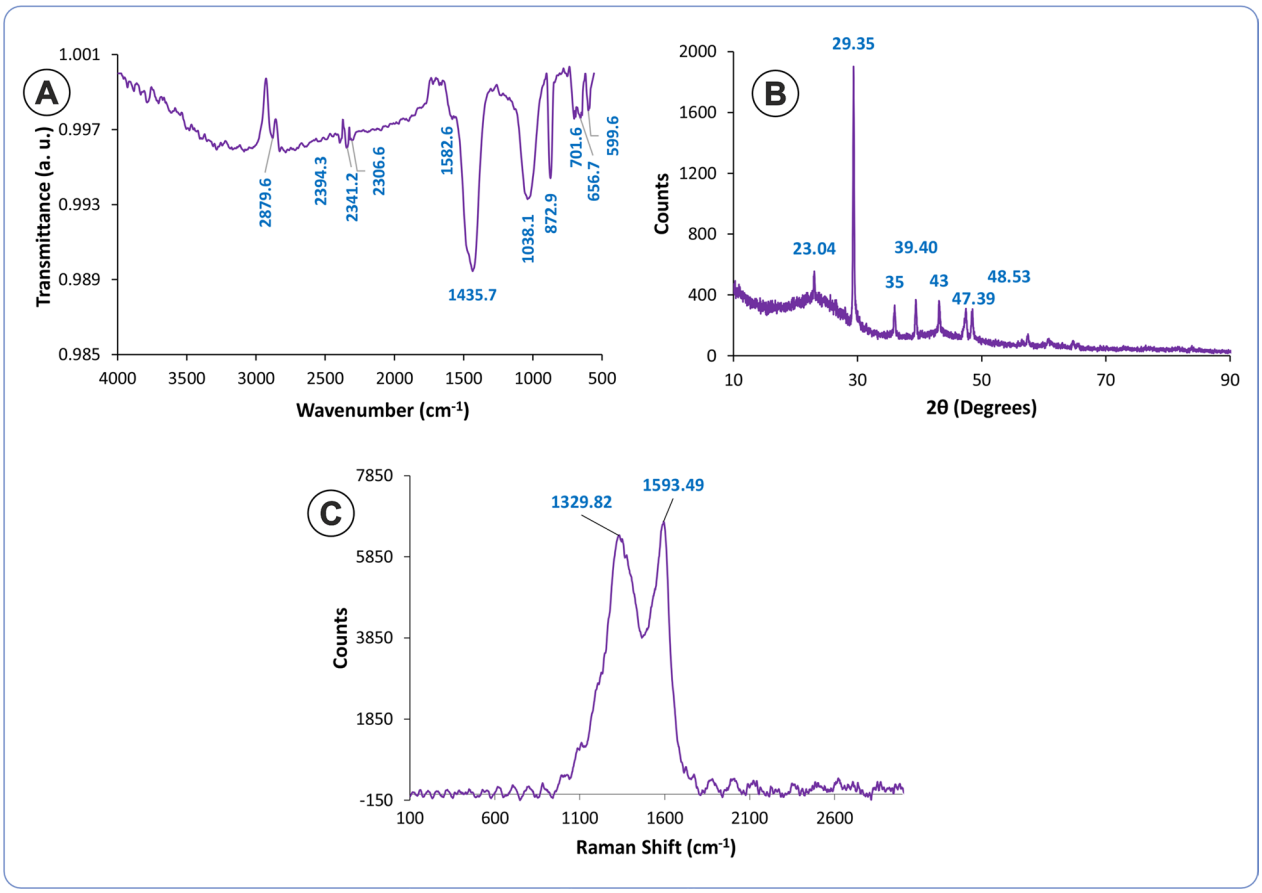

Fig. 3 Surface characterization of JLB: **A** FT-IR, **B** XRD, and **C** Raman spectroscopy

constituents. Raman spectroscopy is particularly sensitive to the molecular arrangement of carbon-rich materials such as biochar. The method can identify nuanced alterations in the arrangement and bonding of carbon atoms, yielding comprehensive insights into the macro- and microstructure of biochar and its level of graphitization (Orlando et al. 2021). Raman spectrum (Fig. 3C) showed that the JLB was a highly graphitic material. This is evident from the presence of the D and G bands of carbon in the spectrum. The D band is associated with defects in the carbon structure, while the G band is associated with the ordered graphite structure (Chen et al. 2020). In this case, the ID/IG ratio was relatively low (0.94), suggesting that the JLB had a high degree of graphitization. In conclusion, the Raman spectrum and XRD analysis indicated that JLB was a highly graphitic material with a low defect density, high surface area, and a variety of functional groups.

XPS provides the analysis of the elemental composition and chemical states of elements present on the biochar surface. A primary advantage of XPS in biochar examination is its capability to detect and characterize surface functional groups (Ilic et al. 2022). XPS analysis for JLB before BG adsorption (Fig. 4I) revealed that the primary constituents of JLB were carbon (C), oxygen (O), and nitrogen (N), with atomic percentages of 78%, 17%, and 5%, respectively. This indicates a carbonaceous material with a significant abundance of oxygen-containing functional groups. The presence of nitrogen suggests the existence of nitrogen-containing functional groups, potentially contributing to BG dye adsorption. The C 1 s spectrum (Fig. 4I–A) showed multiple peaks corresponding to binding energies of 637.5 eV (O=C–O), 398.5 eV (N=C–N), 389.5 eV (N–C=O), 378.5 eV (aromatic rings of carbon), 356.5 eV (C–C) (Kim et al. 2023; Liu et al. 2021). The relative intensities of these peaks suggest a highly oxidized JLB with a substantial amount of oxygen and nitrogen-containing functional groups. The presence of O-C=O indicates oxidation by carboxylic acids or ketones. The presence of N=C-N and N–C=O indicate the different nitrile and amide groups. The O 1 s spectrum (Fig. 4I–C) showed multiple peaks corresponding to binding energies of 882.5 eV (COO), 860.5 eV (C=O,

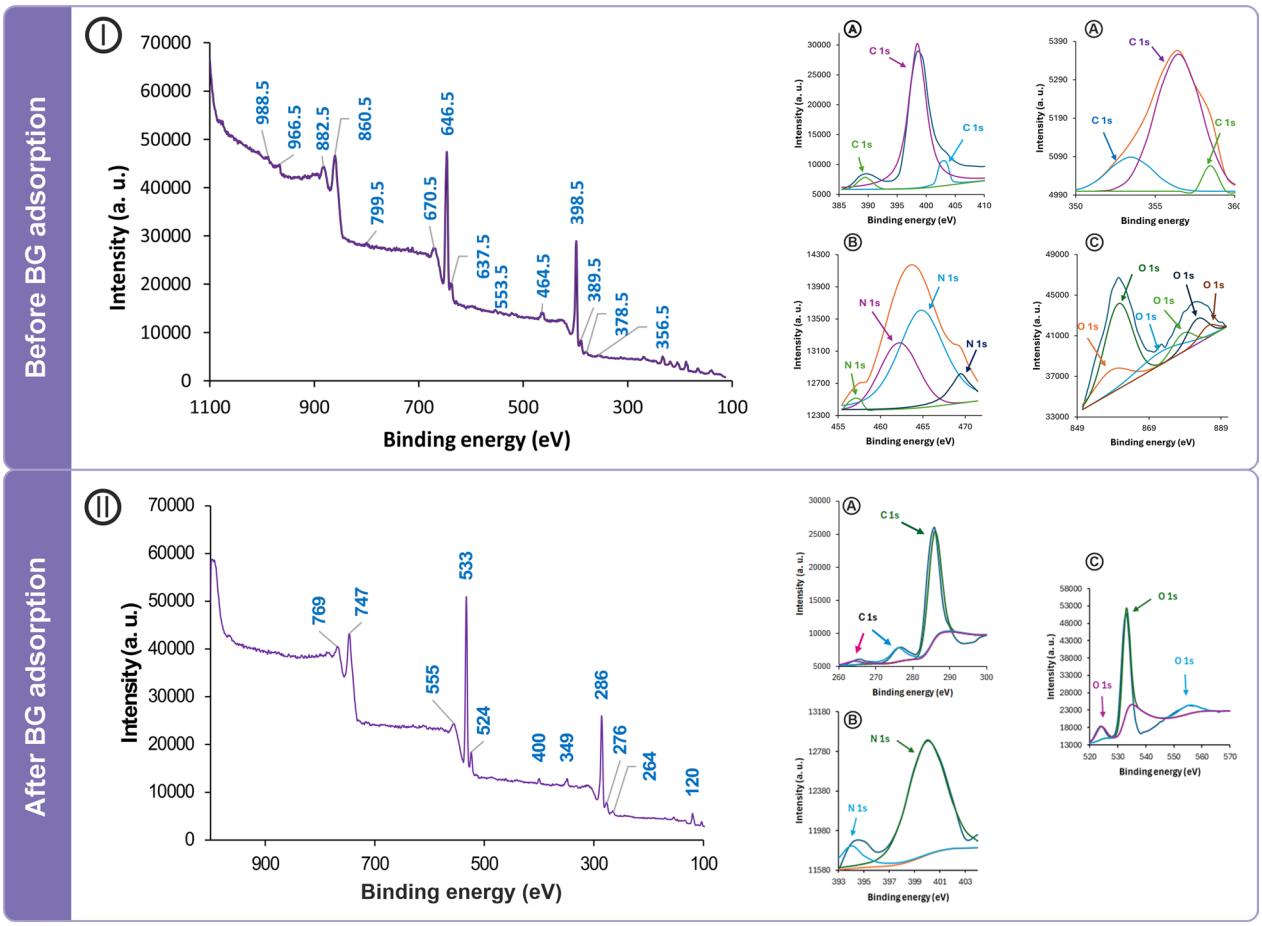

Fig. 4 XPS spectra for the JLB before (I) and after (II) adsorption of BG with deconvolution graphs for carbon (**A**), nitrogen (**B**), and oxygen (**C**)

O-C=O), 799.5 eV (C–O), and O 2 s 553.5 eV (O–C=O) (Liu et al. 2021). These peaks indicate the presence of diverse oxygen-containing functional groups, including hydroxyl groups, carbonyl groups, ether, and carboxylic acid groups. The N 1 s spectrum (Fig. 4I-B) showed two peaks corresponding to binding energies of 988.5 eV (NO_3), 966.5 (NH_3, NH_2), and 464.5 eV (pyridinic N) (dos Reis et al. 2023). These peaks suggest the presence of various nitrogen-containing functional groups, including pyridinic nitrogen, nitrile, and amine groups. The peaks for iron, silica and sulfur were also seen at 670.5 eV (Fe $2p_{3/2,}$), 646.5 eV (Fe $2p_{1/2}$), 218.5 eV (Si 2 s), 188.5 eV (S 2p) (Eltaweil et al. 2020; Santhosh et al. 2020).

The XPS spectrum for JLB after adsorption (Fig. 4II) presented showed several distinct peaks across a binding energy range of approximately 100–1000 eV. The peak at 286, 264, and 276 eV is characteristic of the Carbon (C 1 s) orbital (Fig. 3A). The shift could indicate C-O bonds, which are common in biochar due to oxygen-containing functional groups (Kim et al. 2023). A prominent peak at 533, 524, 555 eV corresponds to the Oxygen (O 1 s) orbital (Fig. 3C). These could include hydroxyl (–OH), carboxyl (–COOH), or carbonyl (C=O) groups (Liu et al. 2018). The peak at 400 eV is indicative of the Nitrogen (N 1 s) orbital (Fig. 3B). This peak is particularly interesting as it likely originates from the BG dye, which contains nitrogen in its molecular structure (Grimm et al. 2023). The presence of this peak confirms the successful adsorption of the dye onto the JLB surface. A small peak at 349 eV can be attributed to the Calcium (Ca 2p) orbital. Calcium is often present in biomass-derived biochar and can act as a binding site for the dye molecules, enhancing the overall adsorption capacity. The peaks at 747 and 769 eV are in the range typically associated with Fe $2p_{3/2}$ and Fe $2p_{1/2}$ spin–orbit splitting, respectively (Santhosh et al. 2020).

In summary, the overall spectrum shape has changed, with some peaks becoming more prominent and others diminishing or disappearing. The C 1 s region showed significant changes. The multiple peaks observed before adsorption (637.5, 398.5, 389.5, 378.5, 356.5 eV) were replaced by fewer, broader peaks at 286, 276, and 264 eV. This suggests a change in the carbon bonding after BG

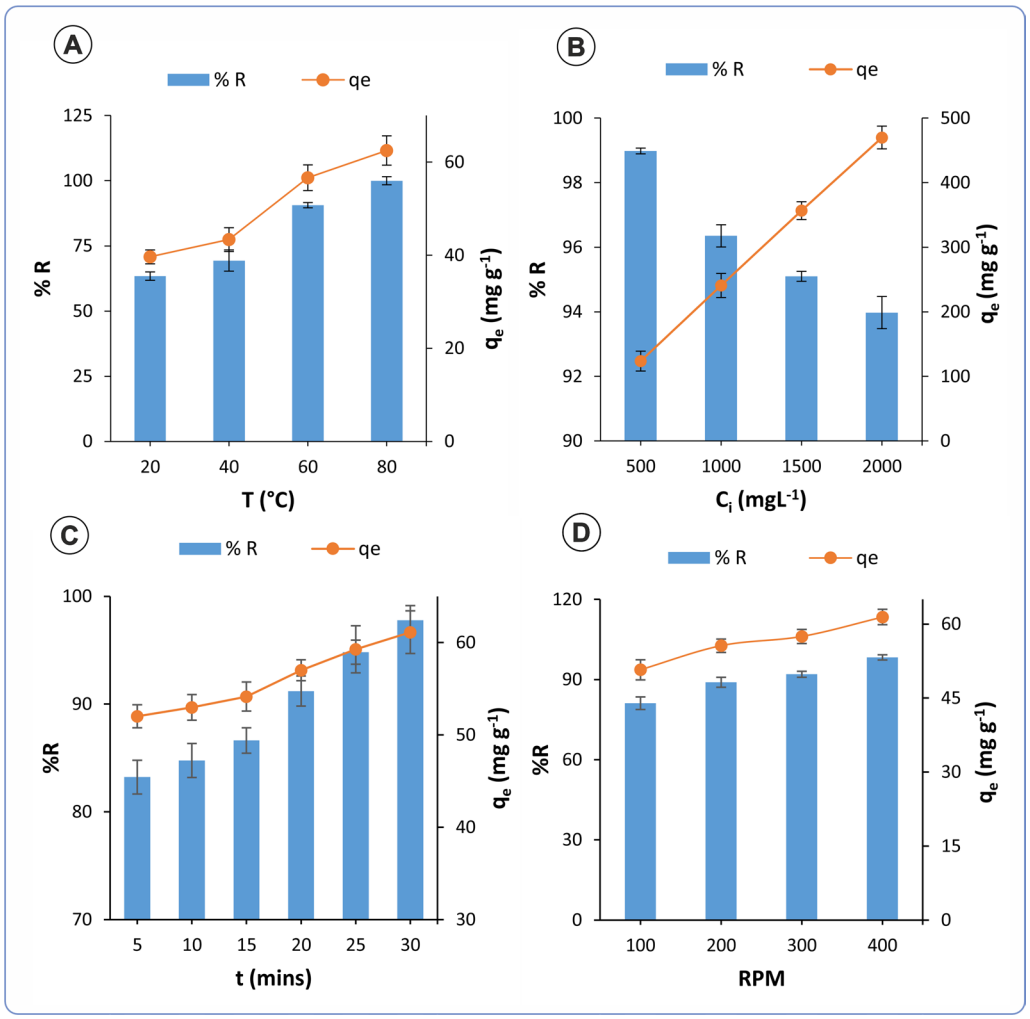

Fig. 5 Optimisation of reaction parameters: **A** temperature (°C), **B** initial concentration (C_i), **C** contact time (t), and **D** agitation

dye adsorption. The distinct O 1 s peaks seen before adsorption (882.5, 860.5, 799.5, 553.5 eV) were replaced by peaks at 555, 533, and 524 eV, indicating a reorganization of oxygen-containing functional groups. In the "before" spectrum, the peaks connected to N 1 s at 988.5, 966.5, and 464.5 eV were no longer visible. These changes indicate significant surface modifications of the JLB after BG dye adsorption, including alterations in functional groups and potential changes in the oxidation states of existing elements. This suggests a complex interaction between the biochar surface and the BG molecules during the adsorption process.

3.2 Batch adsorption studies

3.2.1 Optimization

Figure 5 depicts the effect of temperature (A), initial concentration (B), contact duration (C), and RPM (D) on the removal efficiency (% R) and adsorption capacity (q_e) of BG dye by JLB. As the temperature increased from 20 to 80 °C, the % R increased from about 63.44 to 99.95%. Similarly, Saghir et al. found the same results in their investigation. According to this study, the adsorption of CR and MB on PSB-900 is more temperature-sensitive, indicating an endothermic nature. This means that the biochar is more effective at removing the dye from the solution at higher temperatures. The q_e also increased with temperature, from about 39.65 to 62.47 mg g^{-1}. This means that the biochar can adsorb more dye molecules onto its surface at higher temperatures. There are a few possible explanations for these observations. One possibility is that the adsorption process is endothermic, meaning that it requires heat to occur (Saghir et al. 2022). At higher temperatures, there are more molecules of dye with enough kinetic energy to overcome the energy barrier to adsorption. Another possibility is that the higher temperature opens up more binding sites on the biochar

surface for the dye molecules to attach to (Adeogun et al. 2018). The increase in adsorption capacity with temperature is consistent with the findings of other studies on the adsorption of dyes onto biochars. For example, a study by Pandey et al. noticed that the adsorption capacity of biochar for methylene blue dye elevated as temperature elevated. This could be due to the swelling of the internal structure of adsorbent with higher temperatures, allowing more dye to penetrate further (Pandey et al. 2022). Sun et al. investigated that the removal of MB by adsorption onto biochar increased by increasing the temperature of the solution from 30 to 50 °C (Bulut and Aydin 2006; Sun et al. 2015). Hameed and Ahmad reported that the q_e of MB rose from 82.64 to 142.86 mg g^{-1} when the solution temperature elevated from 303 to 323 K (Hameed and Ahmad 2009). This is similar to other reports where the adsorption rate increases with an increase in temperature (Das et al. 2021; Üner et al. 2016).

As the initial concentration of the dye (C_i) increased from 500 mg L^{-1} to 2000 mg L^{-1}, the % R decreased from 98.98 to 93.97% (Fig. 5B). This means that the JLB was less effective at removing the dye from the solution at higher concentrations. However, the q_e increased with increasing C_i, from about 123.73 to 469.88 mg g^{-1}. Similar results were observed, where the adsorption capacity of MB improved from 208.1 to 384.2 mg g^{-1}, and it increased as the initial dye concentration increased from 50 to 200 mg L^{-1} (Saghir et al. 2022). This means that the biochar can adsorb more dye molecules onto its surface at higher concentrations (Aichour et al. 2022). There are a few possible explanations for these observations. One possibility is that the available binding sites on the biochar surface become saturated at higher dye concentrations. This means that there are not enough sites available for all of the dye molecules to attach to, so some of the dye molecules remain in the solution (Bankole et al. 2024; Tcheka et al. 2024; Tulashie et al. 2022). Another possibility is that the mass transfer of the dye molecules from the solution to the biochar surface becomes limited at higher concentrations. This means that the dye molecules have difficulty reaching the binding sites on the biochar surface, so the adsorption process slows down (Ani et al. 2023; Sangsuk et al. 2023; Yao et al. 2020). The decrease in removal efficiency with increasing concentration is consistent with the findings of other studies on the adsorption of dyes onto biochars. For example, a study by Yang et al. found that the removal efficiency of BR46 dye onto CMBSR (*Chrysanthemum morifolium* Ramat straw biochar) samples decreased as the initial concentration of BR46 dye increased (Yang et al. 2021). An investigation by Das et al. observed that with an increase in initial MG (Malachite Green) concentration, the final MG concentration in the solution increased, resulting in a decrease in adsorption efficiency. The increase in adsorption capacity with increasing concentration is due to the phenomenon of "concentration gradient driving force" (Das et al. 2021). At higher concentrations, there is a greater driving force for the dye molecules to move from the solution to the biochar surface, which results in more dye molecules being adsorbed (Adeogun et al. 2018; Pinky et al. 2023).

As the contact time increased from 5 to 30 min, the % R increased from about 83.22 to 97.79% (Fig. 5C). This means that the biochar is more effective at removing the dye from the solution with longer contact times (Aichour et al. 2022). The q_e also increased with the increasing contact time, from about 52.01 to 61.11 mg g^{-1}. This means that the biochar can adsorb more dye molecules onto its surface with longer contact times (Tcheka et al. 2024; Saghir et al. 2022). There are a few possible explanations for these observations. One possibility is that it takes time for the dye molecules to diffuse from the bulk solution to the biochar surface and then attach to the binding sites. With longer contact times, more dye molecules have the opportunity to reach the biochar surface and be adsorbed (Ani et al. 2023). Another possibility is that the adsorption process is limited by the rate at which the dye molecules can attach to the binding sites on the biochar surface. With longer contact times, there is more time for the dye molecules to attach to the binding sites, which leads to a higher adsorption capacity (Adeogun et al. 2018). The increase in removal efficiency with increasing contact time is consistent with the findings of other studies on the adsorption of dyes onto biochars. For example, a study by Yang et al. found that the removal efficiency of BR46 dye onto CMRSB increased as the contact time increased (Yang et al. 2021).

As the RPM increased from 100 to 400, the % R increased gradually, reaching a maximum value of around 98.28% at 400 RPM (Fig. 5D). This indicates that higher agitation speeds enhance the mass transfer of dye molecules towards the biochar surface, promoting greater adsorption (Aulia et al. 2021). Similar to the % R trend, the q_e also increased with increasing RPM, reaching a maximum value of approximately 61.42 mg g^{-1} at 400 RPM. This further corroborates the notion that higher agitation facilitates more dye molecule attachment onto the binding sites of biochar. Increased RPM translates to a stronger mixing force within the solution, leading to better dispersion of dye molecules. This facilitates their movement towards the biochar surface, overcoming diffusional limitations and promoting adsorption (Fil and Ozmetin 2012). Higher agitation creates a thinner boundary layer surrounding

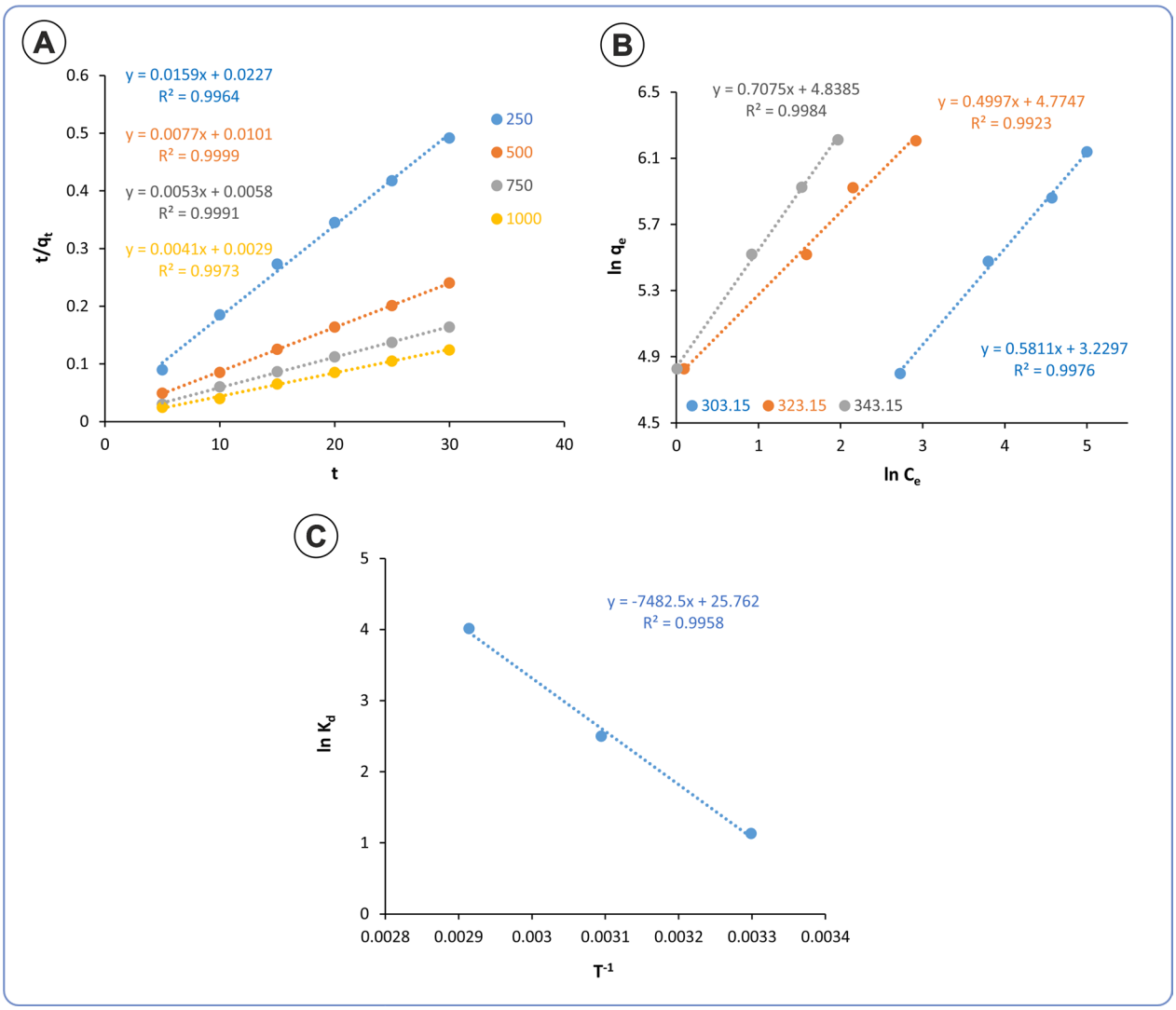

Fig. 6 **A** The fitted pseudo-second-order kinetic model for JLB at different BG concentrations **B** The fitted Freundlich isotherm model for JLB at different temperatures and **C** Thermodynamics graphs for brilliant green adsorption on JLB

the biochar particles. This minimizes the diffusion distance for dye molecules to reach the adsorption sites, thereby accelerating the adsorption process. At higher RPMs, the biochar particles might experience greater collisional encounters. This can dislodge weakly bound dye molecules from the biochar surface, exposing fresh binding sites for further adsorption (Dey et al. 2022). Overall, the results suggest that JLB is a promising adsorbent for the removal of BG from aqueous solutions. In conclusion, the JLB was most effective at removing the BG dye at higher temperatures (80 °C), longer contact times (30 min), and higher agitation speeds (400 RPM).

3.2.2 Kinetics

For BG adsorption, the JLB conformed more closely to the PSO kinetic model than to the PFO (Fig. S2), IPD (Fig. S3), and LFD model (Fig. S4). Figure 6A illustrates the linear representations of PSO kinetic models. Table 1 presents the kinetic variables obtained for the BG adsorption on JLB. The PSO kinetic model is commonly employed to characterize the adsorption kinetics of adsorbates, including dyes, onto adsorbents such as biochar. This model posits that the rate-limiting step is chemisorption, which entails valence forces through the sharing or exchange of electrons between the dye and biochar (Tomin et al. 2024). The results indicated that the BG was adsorbed onto the JLB

Table 1 Adsorption kinetic parameters of BG on JLB

Kinetic model	C_o, mg L^{-1}			
	250	500	750	1000
Pseudo-first order				
$q_{e\,exp}$, mg g^{-1}	60.99	124.77	182.82	241.06
$q_{e\,cal}$, mg g^{-1}	16.82	28.09	107.82	76.83
k_1, g mg^{-1} min^{-1}	0.217	0.326	0.391	0.314
R^2	0.90	0.86	0.93	0.95
Pseudo-second order				
$q_{e\,cal}$, mg g^{-1}	62.89	129.87	181.81	243.90
k_2,g mg^{-1} min^{-1}	0.011	0.0058	0.0052	0.0057
h, mg g^{-1} min^{-1}	44.05	99.00	172.41	344.82
R^2	0.99	0.99	0.99	0.99
Intra-Particle Diffusion				
k_{id},mg g^{-1} $min^{-0.5}$	2.631	6.611	9.959	12.35
C, mg g^{-1}	46.16	91.55	131.80	177.87
R^2	0.92	0.83	0.94	0.80
Liquid Film Diffusion				
k_{fd}, min^{-1}	0.095	0.178	0.176	0.120
C_L	1.24	0.750	0.59	1.30
R^2	0.84	0.93	0.93	0.93

Table 2 Adsorption isotherm parameters of BG on JLB

Isotherm model	C_o, 500–2000 mg L^{-1}		
	303.15 K	323.15 K	343.15 K
Freundlich			
K_f, mg g^{-1}	24.49	114.18	121.19
1/n	0.58	0.49	0.7
R^2	0.99	0.99	0.99
Langmuir			
b, mg g^{-1}	0.013	0.15	0.13
q_m, L g^{-1}	666.66	666.70	1000
R^2	0.97	0.96	0.98
D-R			
q_{DR}, mg g^{-1}	347.32	361.39	407.14
β, m mol^2 J^{-2}	0.00004	0.0000004	0.0000003
R^2	0.85	0.82	0.91
Temkin			
A_T, L mg^{-1}	1.64	4.23	5.88
B_T, L mg^{-1}	8.71	29.85	27.18
R^2	0.96	0.95	0.97

surface following PSO kinetics ($R^2 = 0.99$), suggesting that the process is chemisorption (Ahmad et al. 2020). The results indicated that the rate-limiting variable in the process of adsorption is the charged functional groups on the JLB surface, their specificity for BG, and the mesoporous nature of JLB. For JLB, the q_e value exhibited an exponential rise as the concentration rose from 250 to 1000 mg L^{-1}. According to Tomin et al., this could be caused by bulk diffusion, intraparticle, and pore-filling (Tomin et al. 2024). This is due to several aspects, including the presence of active functional groups specific to BG, an increased surface area conducive to BG adsorption, and a larger pore volume and size. The initial phase of adsorption corresponds to the diffusion of BG through the macropores and mesopores in biochar, whilst the subsequent phase signifies the diffusion of BG through micropores (Nath et al. 2021). The results substantiate previous findings, demonstrating that the chemisorption mechanism constitutes a phase of the adsorption process that governs the rate (Grimm et al. 2023; Mishra et al. 2023; Yazdani et al. 2019, 2016).

At a concentration of 1000 mg L^{-1}, JLB exhibited a q_e value of 243.90 mg g^{-1}, the highest among all initial dye concentrations. The experimental q_e values of JLB were almost perfectly matched by the q_e values projected from PSO kinetic models. Consequently, extensive surface area, substantial pore volume, and prominent mesopores of JLB facilitated efficient BG adsorption with minimal diffusion resistance (Ahmed et al. 2019).

3.2.3 Isotherm and Thermodynamics

The Freundlich and Langmuir adsorption models are commonly used to describe the adsorption of dyes onto biochar and other adsorbents. The Freundlich isotherm is an empirical model that describes heterogeneous surface adsorption. It assumes that adsorption occurs on a heterogeneous surface with sites that have different energies of adsorption (Daffalla et al. 2024). The Langmuir isotherm assumes monolayer adsorption on a surface with a finite number of identical sites. Once a site is filled, no further adsorption can occur at that site (Melo et al. 2023). Figure 6B depicts the isothermal graphs for BG adsorptions on the surface of JLB. Table 2 includes the parameters acquired from various isothermal models. According to the observed high correlation coefficients ($R^2 = 0.99$), the Freundlich model suited the data better than the Langmuir, D-R, and Temkin isothermal models (Fig. S5, S6, and S7). Accordingly, the adsorption of BG on JLB was a process of heterogeneous adsorption with varied distributions of porosity as well as functional groups. Unlike the Langmuir model, the Freundlich model accounts for the heterogeneity of the surface. This means it is more suitable for materials like biochar, which often have a diverse range of adsorption sites and energies (Velić et al. 2023).

The K_f value for the JLB had a linear relationship with temperature, suggesting the impact of temperature on adsorption. The same outcomes were seen in a previous study by Mansour et al. which confirmed the endothermic nature of the retention step by showing an increase in BG dye uptake by activated carbon with temperature (Mansour et al. 2020). This is due to several factors, including the following: 1. As the temperature rises, the viscosity of the water decreases, weakening the link between the water and the BG and creating space for the BG to bind to the JLB. The increased b value may be due to the altered viscosity of water. 2. It's possible that as the temperature rises, the thermal energy causes the functional groups specific to BG to activate. 3. The biochar porosity may be affected by heat energy; micropores may have changed into mesopores and mesopores into macropores, increasing pore size and volume (Mian et al. 2023). This might have facilitated the diffusion of BG molecules into pores and enabled simultaneous pore filling and intraparticle diffusion.

In light of this fact, we would like to explain the "Theory of Pore Conflation" as a possible explanation. Figure 7, 8, and 9 provide data for the "Theory of Pore Conflation". Assuming monolayer adsorption, a single pore can typically accommodate one dye molecule in volume at room temperature. When the temperature continues to rise, the thin border walls of some pores may eventually break and merge with pores that are adjacent to them. This will result in an enlarged volume and increased exposure of functional groups to the surface. In accordance with this hypothesis, as the pore volume grows, more functional groups can engage with dye molecules due to an increase in the accessible space for them. As a result, adsorption efficiency and capacity are enhanced. This theory holds for heterogonous surfaces as well. In the pore-filling mechanism, the fragile pore tunnel wall borders tear and merge to generate a swollen structure known as a pore nodule. The functional groups are exposed to a greater number of dye molecules within the interior of the pore nodules, and the larger volume that comes from this leads to increased adsorption. These nodules can be considered the active regions of biochar for dye adsorption. These pore nodules decrease the probability that dye molecules will block pores, facilitating pore filling

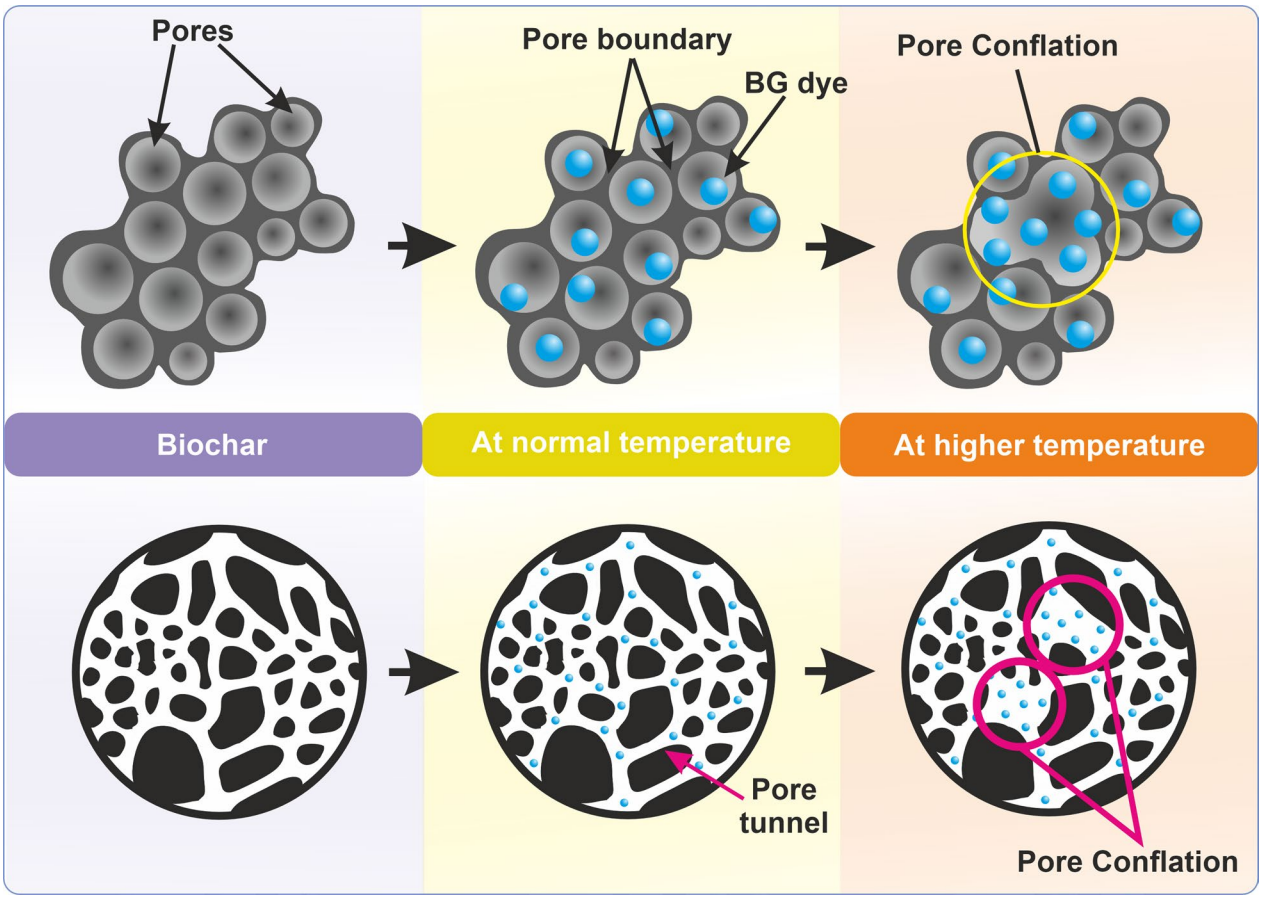

Fig. 7 A schematic depiction of the Pore Conflation Theory

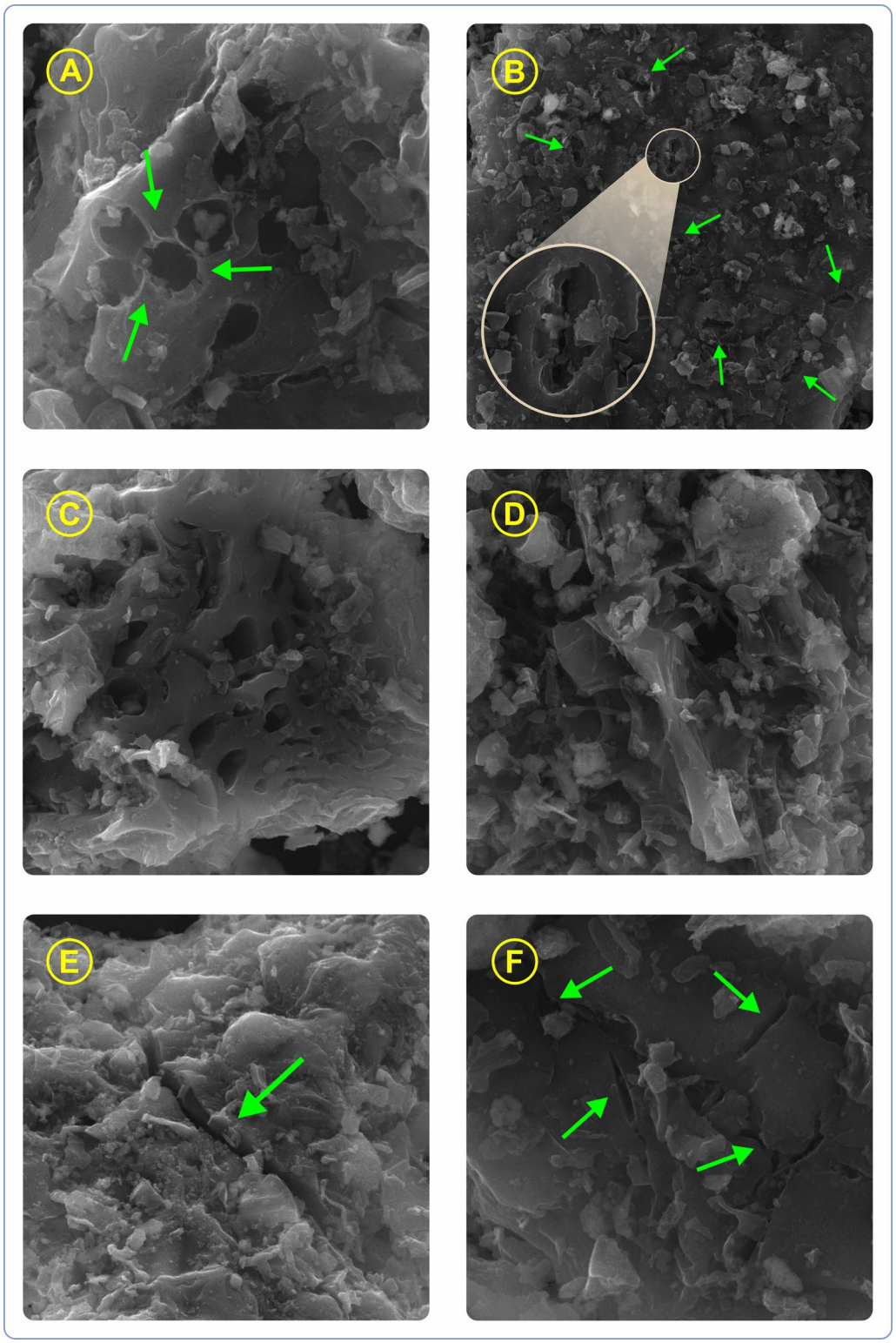

Fig. 8 SEM analysis for JLB heated at 80 °C in an aqueous medium; **A** Pore boundaries tearing, **B** Pore conflation, **C** Pore tunnels, **D** Distorted surface layer, and **E**, **F** Surface cracks

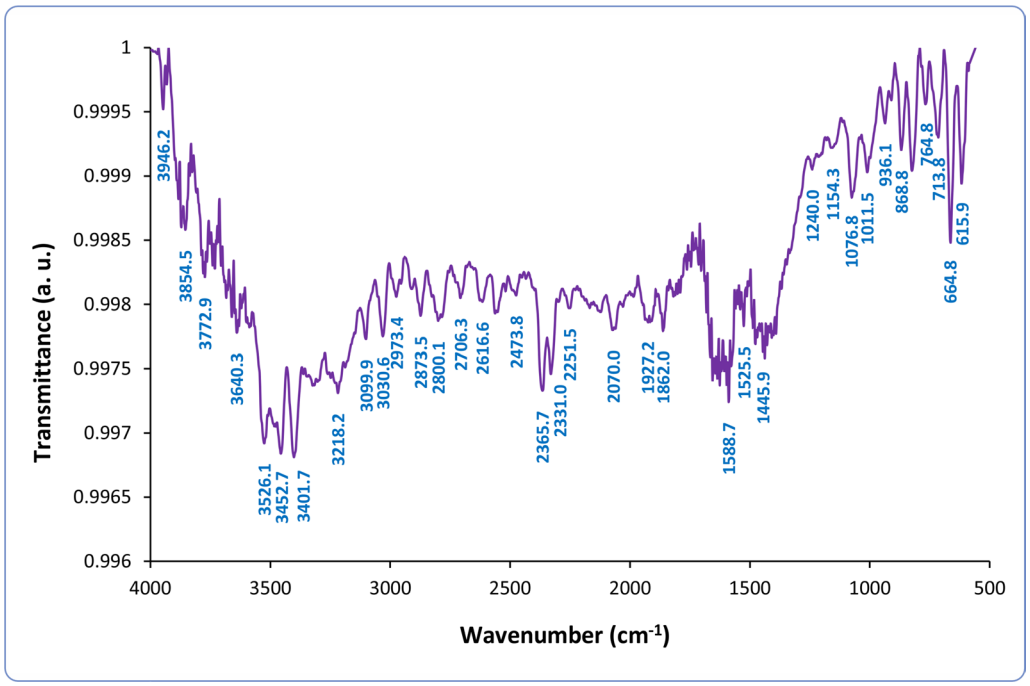

Fig. 9 FTIR analysis for JLB heated at 80 °C in an aqueous medium

and intraparticle diffusion. In the process of dye adsorption, the size and volume of pores, number of pores, functional groups, and length and diameter of the pore tunnel are all crucial. The presence of sufficient volume to accommodate the dye molecule, enough space for dye interaction, and active functional groups for bonding is considered characteristics of an active pore or active site, while the absence of these characteristics is considered indicative of an inactive pore or inactive site. There are occasionally locations in the pores or on the surface of the biochar where there are more function groups, and these sites serve as active adsorption sites. These areas were previously considered to be "active centers," but the explanations of active centers in existing reports are only applicable to functional groups (Pandey et al. 2022). Overall, the adsorption capacity of biochar is a complex phenomenon that is influenced by a variety of factors. Our "Theory of Pore Conflation" is a promising explanation for the enhanced adsorption capacity of biochar at high temperatures. Furthermore, an experiment was conducted to validate this theory, in which biochar was subjected to heating in water at a temperature of 80 °C. Subsequently, the examination of FTIR and SEM was carried out. To observe the alterations in functional groups under elevated temperatures, FTIR was conducted. To observe the changes in the porosity of the biochar, SEM was performed.

The SEM analysis of JLB at 80 °C is presented in Fig. 8, showcasing the effects of high temperature on the pore structure and surface morphology. Figure 8A and B images illustrate the phenomenon of pore tearing. The green arrows highlight the areas where the pore boundaries have torn, causing adjacent pores to merge. This merging (pore conflation) resulted in the formation of larger pores, which significantly increases the surface area available for interaction with the external environment. In Fig. 8B, the magnified section clearly shows the conflation of pores and the formation of pore tunnels. These tunnels were deformed and appeared to be merged, further contributing to increased surface area and exposure of functional groups. Figure 8C image provides a closer look at the contorted structures of the pore tunnels. The irregular and twisted formations suggested significant structural changes due to the elevated temperature. These contorted tunnels indicated an increased complexity in the pore network, which can enhance the interaction between JLB and BG dye molecules.

Fragmentation and disintegration of pores are evident in the image of Fig. 8D. The surface layer showed signs of distortion, with clear fragmentation indicating that the high temperature has caused the JLB to break down at a microstructural level. This fragmentation contributes to the creation of new structures and channels within the material, potentially improving its capacity for the adsorption and transport of dye molecules. In Fig. 8E and

F green arrows point to cracks on the surface of the JLB. These cracks are particularly significant as they facilitate the transport of BG dye molecules, allowing them to penetrate deeper into the JLB material. The cracks also enable pore filling and intraparticle diffusion, which are crucial for effective adsorption. The presence of these cracks indicates that the high temperature has not only increased the pore size but also created additional routes for molecule transport, enhancing the overall adsorption capacity of the JLB. Following are the major functional groups observed in FTIR when biochar was heated at 80 °C (Fig. 9):

1. Hydroxyl Groups (O–H, peaks around 3946.2, 3854.5, 3772.9, 3640.3, 3526.1, 3452.7, 3401.7 cm^{-1}): These peaks were quite prominent, suggesting a significant presence of hydroxyl groups (Hua et al. 2023).
2. Aromatic Compounds (C–H stretching, peaks around 3099.5, 3039.6 cm^{-1}; C=C stretching, peaks around 1588.7, 1525.5 cm^{-1}): These peaks were moderate in intensity, indicating a moderate presence of aromatic compounds (Tcheka et al. 2024).
3. Aliphatic Hydrocarbons (C–H stretching, peaks around 2870.5, 2801.5, 2706.3, 2616.6, 2473.8 cm^{-1}): These peaks were relatively less intense, suggesting a lower presence of aliphatic hydrocarbons (Aichour et al. 2022).
4. Carbonyl Groups (C=O, peak around 1862.0 cm^{-1}): This peak was relatively weak, indicating a low presence of carbonyl groups (Muniasamy et al. 2024).
5. Other Functional Groups (C≡C or C≡N, peaks around 2255.7, 2170.2 cm^{-1}; C–O stretching and bending vibrations, peaks around 1240.0, 1154.3, 1076.8, 1011.5 cm^{-1}): The peaks in this region varied in intensity, suggesting a variable presence of these functional groups (Hua et al. 2023).

At 80 °C, there's increased differentiation in the O–H and N–H stretching region (3000–3600 cm^{-1}), suggesting more available hydroxyl and amine groups. This could have enhanced hydrogen bonding with BG dye molecules. The appearance of a new carbonyl peak (1862 cm^{-1}) at 80 °C indicates increased oxygen-containing functional groups, which could have improved electrostatic interactions with the dye. Changes in the aromatic C=C stretching (around 1580–1590 cm^{-1}) and C-H bending regions (600–900 cm^{-1}) suggest increased aromaticity at 80 °C, potentially enhancing π-π interactions with the aromatic structure of BG.

In summary, the SEM analysis at 80 °C revealed that high temperature induced significant changes in the pore structure and surface morphology of JLB. The pore conflation, formation of contorted pore tunnels, fragmentation, and surface cracks all contribute to an increased surface area and improved interaction with BG dye molecules. The abundance of hydroxyl, carboxyl, and phenolic groups suggested that JLB had a significantly increased negative surface charge, primarily due to the dissociation of acidic functional groups (e.g., –OH and –COOH) and the presence of ionizable phenolic groups (Wei et al. 2022). The presence of carbonyl groups and ether/ester groups further influenced the overall polarity and electron distribution of biochar, contributing to its adsorption properties and chemical reactivity (Park et al. 2021).

Table 3 presents the thermodynamic parameters of BG adsorption onto JLB. Figure 6C illustrates the linear graphs of thermodynamics. The BG adsorption onto the JLB was endothermic and spontaneous, as revealed by the negative ΔG° and positive ΔH° values (Sun et al. 2015). The adsorption of BG onto JLB demonstrated negative ΔG° values at 303.15, 323.15, and 343.15 K, signifying the presence of advantageous spontaneous processes at elevated temperatures. The positive value of ΔH° reinforces the endothermic character of the adsorption process of BG, consistent with the observed increase in q_e with elevated temperature. The positive values of ΔS° during the adsorption mechanism indicate increased randomness at the JLB-BG solution interface (Ding et al. 2015).

3.3 Adsorption mechanism

JLB had a diverse surface with various particle sizes, shapes, and features like large and small pores, cracks, and agglomerates. This variety provides different binding sites for BG molecules. XRD and Raman analysis revealed the presence of a highly graphitic material. JLB possessed a rich collection of functional groups like hydroxyl, carbonyl, aromatic rings, and ether groups. These groups can interact with BG through different mechanisms. XPS analysis highlighted the presence of carbon, oxygen, and nitrogen, indicating a carbonaceous material with oxygen-containing functional groups. Large surface area and diverse pore network of biochar facilitate easier access and deeper penetration of BG molecules (Gong et al. 2020; Zeng et al. 2021; Zhang et al. 2023).

Table 3 Adsorption thermodynamic parameters of BG on JLB

ΔH°, kJ mol^{-1} K^{-1}	ΔS°, kJ mol^{-1} K^{-1}	ΔG°, kJ mol^{-1}		
		303.15 K	323.15 K	343.15 K
11.25	3.72	– 4.71	– 79.29	– 153.88

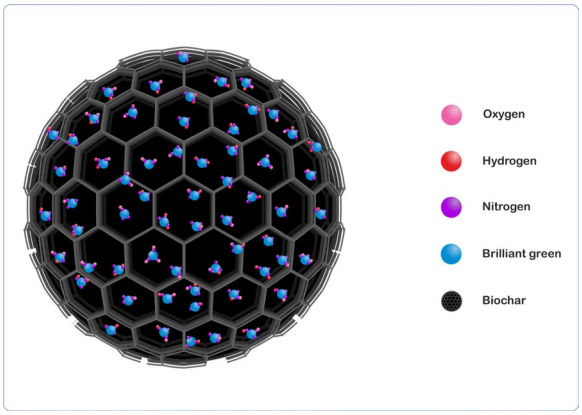

Fig. 10 Unveiling the Adsorption Process of BG on JLB: A Proposed Mechanism

The predicted binding mechanism is as follows (Fig. 10):

a. Hydrogen bonding: Hydroxyl and carbonyl groups on JLB can form hydrogen bonds with the amine groups on BG, leading to strong electrostatic attraction (Aichour et al. 2022).
b. π-π stacking: Aromatic rings on both JLB and BG can interact through π-π stacking, inducing planar interactions and further adsorption (Chen et al. 2020).
c. Dipole–dipole interactions: Ether groups on JLB can engage in dipole–dipole interactions with the negatively charged sulfonic groups of BG (Ghosh et al. 2023).
d. Chemisorption: The pseudo-second-order kinetic model suggests chemisorption as the dominant mechanism. This involves electron sharing between functional groups on JLB and BG, forming strong covalent bonds (Grimm et al. 2023; Ahmad et al. 2020).

Overall, the adsorption of BG onto JLB is a complex process driven by multiple interactions between diverse functional groups and the porous structure of the biochar. Chemisorption plays a significant role, and various factors can influence the efficiency of the process.

3.4 Shubhjyot's equation model

Despite the fact that time plays a significant role in the adsorption process, it has been overlooked in the equations that have been used to calculate adsorption capacity, as can be seen in the following equations (Eq. 1 and 2),

$$q_e = \frac{(C_o - C_e)\, V}{W}$$

$$q_t = \frac{(C_o - C_t)\, V}{W}$$

Previously, scientists calculated the q_e and q_t values, which calculate the adsorption capacity for a particular adsorbent material. However, these equations do not help to understand the importance of time during the adsorption process. The unit for q_e is mg g^{-1}. To better understand the role of time in the adsorption process, we need to add time to it. Using Shubhjyot's equation, we will have a better understanding of the following objectives.

1. It allows us to account for the fact that the adsorption capacity of an adsorbent is not constant over time. As time progresses, the surface of the adsorbent becomes more saturated with the adsorbate, and the adsorption capacity decreases.
2. It can help us to determine the saturation time of a particular adsorbent at a particular concentration of dye and adsorbent, volume of solution, and time.
3. It can help us to predict the equilibrium adsorption capacity of a material, i.e. the maximum amount of adsorbate that can be adsorbed onto the adsorbent.
4. It can help us to optimize the adsorption process by determining the optimum time for the adsorption to take place.

To further understand how time affects the adsorption process, we revised the previous equations by adding time. The transient adsorption capacity (q_r) has been determined in relation to time.

The equation can be derived from the following:

1. q_r α 1/t: This suggests that the adsorption capacity is inversely proportional to time. As the adsorption process takes place, the active sites on the adsorbent become saturated with adsorbate molecules as time goes up. Once all of the active sites are filled, no more adsorption can take place.
2. q_r α 1/W: This means that the adsorption capacity is inversely proportional to the mass of the adsorbent. This is because the amount of substance adsorbed will decrease with the mass of the adsorbent, as there is less surface area for the adsorbate molecules to adsorb onto.
3. q_r α V: This implies that the adsorption capacity exhibits a direct relationship with the volume of the solution. This phenomenon can be attributed to the positive correlation between the volume of the solution and the quantity of substance adsorbed. This relationship arises from the greater availability of adsorbate molecules for adsorption as the solution volume increases.
4. q_r α C_o—C_t: This means that the adsorption capacity is directly proportional to the difference between

the initial (C_o) and the equilibrium (C_e) or at a particular time (C_t) concentration of the adsorbate. This is because the amount of substance adsorbed will increase with the difference between the initial and equilibrium concentrations, as there are more adsorbate molecules available to be adsorbed.

By combining these equations, we get the following Shubhjyot's equation for the Transient adsorption capacity:

$$q_r \cdot \alpha \cdot 1/t \times 1/W \times V \times (C_o - C_t).$$

which can be simplified to the following equation:

$$q_r = \frac{(C_o - C_t)\, V}{W\, t}$$

as,

$$q_t = \frac{(C_o - C_t)\, V}{W}$$

Combine these two equations to express q_r in terms of q_t and t:

$$q_r = \frac{q_t}{t}$$

Simplifying the above equation,

$$\frac{1}{q_r} = \frac{t}{q_t}$$

Or

$$\frac{1}{q_r} = \frac{1}{q_t}\, t \tag{24}$$

For equilibrium time, the equation will be as follows,

$$\frac{1}{q_r} = \frac{1}{q_e}\, t \tag{25}$$

q_r is the transient adsorption capacity (mg g^{-1} min^{-1}). The linear plot of $1/q_r$ vs. t was plotted and the q_t and q_e values were calculated from the slope. This relationship indicates that as time increases, the transient adsorption capacity decreases (inversely proportional), and it is also dependent on the adsorbed quantity at that specific time.

For BG adsorption, JLB suited Shubhjyot's equation model with consistent $R^2 = 0.99$ to all the concentrations (250–1000 mg L^{-1}). Figure 11 depicts the linear plots for Shubhjyot's model. Table 4 displays Shubhjyot's equation parameters acquired for the BG adsorption on JLB. The fact that the observed q_e value and the calculated q_e value from Shubhjyot's equation plot were reasonably near to each other suggests the model fit. The q_r value, declined linearly as the time passed (the Shubhjyot's equation shows that time is inversely proportional to the q_r). This could be because of the accumulation of active sites, slower intraparticle diffusion, and liquid film diffusion. The highest rate of adsorption, 8.03 mg g^{-1} min^{-1}, was noticed at a concentration of 1000 mg L^{-1}. At all concentrations, the initial rate of adsorption was higher, but it was later reduced. The earliest stages of this might be attributed to bulk diffusion, liquid film diffusion, and surface adsorption, followed by intraparticle diffusion and pore-filling mechanisms. The affinity-driven intraparticle diffusion and pore-filling mechanisms need more time to operate, which explains why the q_r value declined linearly as the time rose.

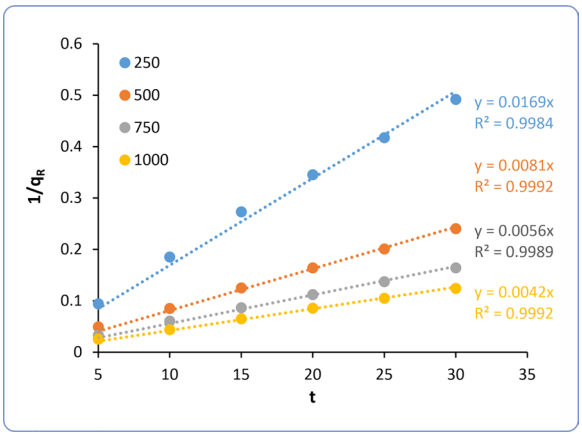

Fig. 11 The fitted Shubhjyot's model for JLB, at different BG concentrations

In addition, Shubhjyot's equation can be used to determine the equilibrium adsorption capacity, which is the maximum amount of adsorbate that can be adsorbed by the adsorbent. This is important because the equilibrium adsorption capacity can be used to design and optimize adsorption processes. This information can be used to optimize the adsorption process by determining the optimum time for the adsorption to take place.

3.5 Desorption studies

This study aims to make the JLB reusable, and use extracted BG dye for different purposes. The combined images and related parameters for the observed desorption investigation are shown in Figure S8 and Table 5. The solubility of BG in organic solvents is significantly higher than that of water. The water is subsequently removed from the system when the adsorption step is completed. There was an interaction between BG and JLB that can be described as a solute-to-solute interaction; however, this contact can be disrupted by the addition of a solvent. The highest desorption efficiency was observed for

Table 4 Transient adsorption capacity rate parameters of BG adsorption on JLB

t = 0–30 min (5 min interval)						
C_o, 250 mgL^{-1}						
$q_{e\ exp}$	**q_t**	**$q_{e\ cal}$**	**R^2**	**q_r**	**$q_{r\ cal}$**	**R^2**
60.99	53.04	62.89	0.99	10.60	59.17	0.99
	53.98			5.39		
	54.91			3.66		
	57.91			2.89		
	59.87			2.39		
	60.99			2.03		
t = 0–30 min (5 min interval)						
C_o, 500 mgL^{-1}						
$q_{e\ exp}$	**q_t**	**$q_{e\ cal}$**	**R^2**	**q_r**	**$q_{r\ cal}$**	**R^2**
124.77	101.45	129.87	0.99	20.29	123.45	0.99
	117.22			11.72		
	119.70			7.98		
	122.0			6.10		
	124.32			4.97		
	124.77			4.15		
t = 0–30 min (5 min interval)						
C_o, 750 mgL^{-1}						
$q_{e\ exp}$	**q_t**	**$q_{e\ cal}$**	**R^2**	**q_r**	**$q_{r\ cal}$**	**R^2**
182.77	150.67	181.81	0.99	30.13	178.57	0.99
	165.28			16.52		
	173.06			11.53		
	178.18			8.90		
	182.01			7.28		
	182.77			6.09		
t = 0–30 min (5 min interval)						
C_o, 1000 mgL^{-1}						
$q_{e\ exp}$	**q_t**	**$q_{e\ cal}$**	**R^2**	**q_r**	**$q_{r\ cal}$**	**R^2**
241.06	195.49	243.90	0.99	39.09	238.09	0.99
	228.0			22.80		
	229.92			15.328		
	233.93			11.69		
	238.03			9.52		
	241.06			8.03		

iso-propanol with 64.05 ± 13.66% compared to methanol and ethanol, 43.85 ± 22.83 and 52.69 ± 23.66%.

The adsorption capacity of JLB remained constant for the first five cycles before reaching saturation. The desorption capacity increased linearly (q_d = 38.43 to 32.65 mg g^{-1}), suggesting that there are more dye molecules on JLB. In comparison to the desorption potential of isopropanol, the dye and JLB interaction was revealed to be stronger at saturation point. Desorption is a time-dependent process (Table 5); therefore, if the duration is extended at the saturation point, the contact between the dye and the JLB will loosen, and the desorption potential of isopropanol will increase. This will lead to an increase in the desorption cycles for BG from JLB (Mandal et al. 2017; Santhosh et al. 2020).

Table 5 Desorption study parameters for the desorption of BG from JLB

Solvent	C_d	q_d	% D
Methanol	105.24 ± 54.80	26.31 ± 13.70	43.85 ± 22.83
Ethanol	126.45 ± 56.77	31.61 ± 14.19	52.69 ± 23.66
Isopropanol	153.73 ± 32.78	38.43 ± 8.19	64.05 ± 13.66
Cycles (Isopropanol)			
I	153.73 ± 32.78	38.43 ± 8.19	64.05 ± 13.66
II	168.88 ± 45.76	42.22 ± 11.44	70.37 ± 19.07
III	187.06 ± 91.06	46.77 ± 22.77	77.94 ± 37.94
IV	190.09 ± 157.46	47.52 ± 39.36	79.20 ± 65.61
V	196.15 ± 130.58	49.04 ± 32.65	81.73 ± 54.41

The findings align with research on biochar as an adsorbent for dyes in aqueous environments, emphasizing its eco-friendly and economical nature for removing toxic dyes. The ability of biochar to adsorb and desorb dyes efficiently was highlighted, showcasing its potential for water treatment applications (Srivatsav et al. 2020).

3.6 Phyto-toxicity

The inhibition percentage of germination for BG was 76.66%, indicating its effect on seed germination. In comparison to the control shoot and root lengths (19.12 ± 1.11 and 5.09 ± 1.08 cm, respectively), 76.66% of the grown seeds exhibited substantially decreased shoot and root lengths (10.96 ± 1.70 and 3.89 ± 0.30 cm, respectively). It displays the cell-level impacts of BG, which disrupt the growth phases of the plant root and shoot cells, resulting in reduced growth. Both the shoot and the root exhibited relatively low-stress tolerance capacities (57.33% and 76.33%, respectively). This indicates that the plant roots and shoots are more susceptible to BG because of their low-stress tolerance index, resulting in comparatively short shoot and root lengths. The content of chlorophyll a and b (9.65 ± 8.82 and 56.82 ± 11.60 mg g^{-1}, respectively) was considerably lower than that of the control (13.84 ± 8.10 and 81.30 ± 22.05 mg g^{-1}, respectively), indicating the detrimental impact of BG on the photosynthesis process (Bedekar et al. 2015).

Table 6 demonstrates that the JLB exhibited values closely aligned with the control values across all parameters. This indicates that, relative to BG, biochar exerts no adverse effects on the physical growth of plants. This indicates that JLB could potentially be utilized in environmental applications to remediate wastewater contaminated with BG.

3.7 Cyto-genotoxicity

Table 7 presents the variables obtained from the cyto-genotoxicity analysis. The cyto-genotoxicity of water (control) and JLB were assessed to evaluate the toxicity of each sample on *A. cepa* root cells. *A. cepa* root cells, due to their increased susceptibility to sudden environmental alterations, serve as a model for elucidating cellular and genetic alterations.

In the case of BG treatment, metaphase, anaphase, and telophase were not observed. This indicates that the BG dye molecules within the cells have disrupted the proteins essential for the cell to progress into metaphase, resulting in their disintegration. Only a limited number of cells at the interface (3.66 ± 1.52) were seen. This indicates that the primary function of the BG is to obstruct cell division. Apoptotic cells were observed. The nucleus is divided into multiple smaller nuclei (Bedekar et al. 2015). The proportion of aberrant cells (52.33 ± 20.60) was significantly elevated, indicating a substantial degree of mortality. Table 7 indicates that the JLB values were comparable to those of the control group. The BG molecules are very toxic to the root cells of *A. cepa*. The JLB is not significantly detrimental; therefore, they can potentially be utilized in the future for the treatment of wastewater affected by BG contamination.

4 Conclusion

This research data present a comprehensive investigation into the adsorption of BG dye using biochar synthesized from *Syzygium cumini* leaves (JLB). The research

Table 6 Various phytotoxicity assessment parameters for BG adsorption on JLB

	G (%)	SL (cm)	RL	STI (%)		CC (mg g^{-1})		
				SLSTI	RLSTI	Chl. a	Chl. b	Total Chl
Control	100	19.12 ± 1.11	5.09 ± 1.08	–	–	13.84 ± 8.10	81.30 ± 22.05	95.14
JLB	100	18.13 ± 1.28 ^{ns}	4.89 ± 0.37 ^{ns}	94.82	96.14	13.36 ± 1.37 ^{ns}	78.05 ± 12.26 ^{ns}	91.43
Dye	76.66	10.96 ± 1.70 ***	3.89 ± 0.30 ***	57.33	76.33	9.65 ± 8.82 ***	56.82 ± 11.66 ***	66.48

CC = Chlorophyll content, Chl. = Chlorophyll, SL = Shoot length, RL = Root length, SLSTI = Shoot length stress tolerance index, RLSTI = Root length stress tolerance index, STI = Stress tolerance index, G = Germination, I = Inhibition, BG (0.1 gL^{-1}) = Brilliant green, JLB = 0.2 g, NA = Not applicable, ^{ns} = Non-significant. The values are mean of three experiments ± SD (standard deviation) significantly different from control at $*p \leq 0.05$, $**p \leq 0.01$, $***p \leq 0.001$ by one-way analysis of variance (ANOVA) with Dunnett comparison test

Table 7 Comparative analysis of cytogenotoxicity parameters induced by JLB and BG

	G	NOC	No. of cells							%AB	%MI
			P	M	A	T	D	I	AB		
W	Y	100	39.67 ± 7.09	5.00 ± 2.0	4.00 ± 1.00	2.66 ± 1.52	51.33 ± 8.96	48.67 ± 8.96	0	0	51.33 ± 8.96
BG	Y	100	3.66 ± 1.52***	0***	0***	0***	3.66 ± 1.52***	96.33 ± 1.53***	52.33 ± 20.60***	52.33 ± 20.60***	3.667 ± 1.52***
JLB	Y	100	34.33 ± 4.04^{ns}	4.66 ± 1.52^{ns}	3.00 ± 1.00^{ns}	1.33 ± 0.57^{ns}	43.33 ± 7.02^{ns}	56.67 ± 7.02^{ns}	0^{ns}	0^{ns}	43.33 ± 7.02^{ns}

W = Control, NOC = Number of cells counted, G = Germination, P = Prophase, M = Metaphase, A = Anaphase, T = Telophase, I = Interphase cells, AB = Aberrant cells, MI = Mitotic index, Y = Yes, W = Control, BG (5 mgL^{-1}) = Brilliant green, JLB = 0.2 g, ^{ns} = Non-significant. The values are mean of three experiments ± SD significantly different from control at $*p \leq 0.05$, $**p \leq 0.01$, $***p \leq 0.001$ by one-way analysis of variance (ANOVA) with Dunnett comparison test

identified optimal conditions for BG dye adsorption, including temperature (80 °C), initial dye concentration (500 mg L^{-1}), contact time (30 min), and agitation speed (400 RPM). These findings are crucial for practical applications and can guide the design of efficient adsorption systems. The surface characterization of JLB revealed a highly porous and heterogeneous structure, rich in carbon and oxygen, with significant functional groups such as hydroxyl, carbonyl, and aromatic rings. These features contributed to the high q_e of biochar by providing numerous active sites for dye molecules to interact with through various mechanisms, including hydrogen bonding, π-π stacking, dipole–dipole interactions, and chemisorption. The data provided a good fit for the pseudo-second-order kinetics that described the chemosorption process of adsorption. The Freundlich model is supported by isothermal data that clarified the heterogeneous surface and its diverse energy distribution for adsorption. The study introduced the novel "Theory of Pore Conflation," which suggests that as pore volume increases due to the merging of adjacent pores at high temperatures, more functional groups can interact with dye molecules, enhancing adsorption efficiency. The formation of pore nodules by merging walls plays a crucial role in facilitating intraparticle diffusion and preventing pore blockage during dye adsorption. Furthermore, the data present "Shubhjyot's equation" for transient adsorption capacity (q_r), which expands our understanding of the adsorption process by considering the change in adsorption capacity over time, accounting for surface saturation and decreasing capacity. This equation aids in determining saturation time, predicting equilibrium adsorption, and optimizing adsorption processes. Desorption studies showed that the adsorption capacity of JLB remained constant for the first five cycles before reaching saturation. The highest desorption efficiency was observed for isopropanol. The phytotoxicity and cyto-genotoxicity assessments demonstrated that JLB was significantly less hazardous compared to BG dye, indicating its potential for safe application in wastewater treatment without causing adverse effects on the environment or living organisms. The findings suggest that JLB is a promising material for textile dye wastewater treatment, offering a sustainable and effective solution to address the environmental challenges associated with dye pollution.

Supplementary Information

The online version contains supplementary material available at https://doi.org/10.1007/s42773-024-00406-2.

Supplementary Material 1.

Acknowledgements
Shubham Sutar expresses gratitude to the Mahatma Jyotiba Phule Research & Training Institute for awarding the MAHAJYOTI fellowship [Outward No. MAHAJYOTI/Nag./Fellowship/2021-22/1042 (388)]. Prof. Jyoti Jadhav expresses gratitude to the Department of Biotechnology, Government of India, for the assistance received through the Interdisciplinary Program of Life Sciences for Advanced Research and Education (DBT-IPLS, Reference No: BT/PR4572/INF/22/147/2012).

Authors' contribution
Shubham Sutar: Conceptualization, investigation, methodology, formal analysis, visualization, data curation, writing—original draft. Jyoti Jadhav: Conceptualization, validation, resources, review and editing, visualization, supervision.

Data availability
Data will be made available on request.

Declarations

Competing interests
The authors declare that they have no known competing financial interests or personal relationships that could have appeared to influence the work reported in this paper.

Author details
[1]Department of Biotechnology, Shivaji University, Kolhapur 416004, Maharashtra, India.

Received: 2 April 2024 Revised: 11 November 2024 Accepted: 24 November 2024
Published online: 13 January 2025

References

Abdu M, Babaee S, Worku A, Msagati TAM, Nure JF (2024) The development of Giant reed biochar for adsorption of Basic Blue 41 and Eriochrome Black T. azo dyes from wastewater. Sci Rep. https://doi.org/10.1038/s41598-024-67997-5

Adeogun AI, Ofudje EA, Idowu MA, Kareem SO, Vahidhabanu S, Ramesh Babu B (2018) Biowaste-derived hydroxyapatite for effective removal of reactive yellow 4 dye: equilibrium, kinetic, and thermodynamic studies. ACS Omega 3:1991–2000. https://doi.org/10.1021/acsomega.7b01768

Ahmad A, Khan N, Giri BS, Chowdhary P, Chaturvedi P (2020) Removal of methylene blue dye using rice husk, cow dung and sludge biochar: Characterization, application, and kinetic studies. Bioresour Technol. https://doi.org/10.1016/j.biortech.2020.123202

Ahmed MJ, Okoye PU, Hummadi EH, Hameed BH (2019) High-performance porous biochar from the pyrolysis of natural and renewable seaweed (*Gelidiella acerosa*) and its application for the adsorption of methylene blue. Bioresour Technol 278:159–164. https://doi.org/10.1016/j.biortech.2019.01.054

Aichour A, Zaghouane-Boudiaf H, Djafer Khodja H (2022) Highly removal of anionic dye from aqueous medium using a promising biochar derived from date palm petioles: characterization, adsorption properties and reuse studies. Arab J Chem 15:103542. https://doi.org/10.1016/j.arabjc.2021.103542

Aljeboree AM, Alshirifi AN, Alkaim AF (2017) Kinetics and equilibrium study for the adsorption of textile dyes on coconut shell activated carbon. Arab J Chem 10:S3381–S3393. https://doi.org/10.1016/j.arabjc.2014.01.020

Ambaye TG, Vaccari M, van Hullebusch ED, Amrane A, Rtimi S (2021) Mechanisms and adsorption capacities of biochar for the removal of organic and inorganic pollutants from industrial wastewater. Int J Environ Sci Technol. https://doi.org/10.1007/s13762-020-03060-w

Amdeha E (2023) Biochar-based nanocomposites for industrial wastewater treatment via adsorption and photocatalytic degradation and the parameters affecting these processes. Biomass Convers Biorefin. https://doi.org/10.1007/s13399-023-04512-2

Ani MO, Menkiti MC, Aniagor CO, Nworie CE, Ochi DO (2023) *Canarium schweinfurthii* stone-derived biochar: a promising adsorbent for crystal violet dye removal. Results Surf Interf 12:100144. https://doi.org/10.1016/j.rsurfi.2023.100144

Aulia SD, Wijayanti A, Hadisoebroto R (2021) The effect of mixing speed and contact time on dye removal using Cassava Peel adsorbents, IOP Conference Series: Earth and Environmental Science. Institute of Physics. https://doi.org/10.1088/1755-1315/737/1/012013

Bankole DT, Inyinbor AA, Oluyori AP, Arowolo MO (2024) Adsorptive removal of synthetic food dyes using low-cost biochar: efficiency prediction, kinetics and desorption index evaluation. Bioresour Technol Rep 25:101709. https://doi.org/10.1016/j.biteb.2023.101709

Batool F, Qadir R, Adeeb F, Kanwal S, Abdelrahman EA, Noreen S, Albalawi BFA, Mustaqeem M, Imtiaz M, Ditta A, Gondal HY (2023) Biosorption potential of *Arachis hypogaea*-derived biochar for Cd and Ni, as evidenced through kinetic, isothermal, and thermodynamics modeling. ACS Omega 8:40128–40139. https://doi.org/10.1021/acsomega.3c02986

Bedekar PA, Kshirsagar SD, Gholave AR, Govindwar SP (2015) Degradation and detoxification of methylene blue dye adsorbed on water hyacinth in semi continuous anaerobic-aerobic bioreactors by novel microbial consortium-SB. RSC Adv 5:99228–99239. https://doi.org/10.1039/c5ra17345k

Belcaid A, Beakou BH, Bouhsina S, Anouar A (2023) New insights on manganese dioxide nanoparticles loaded on cellulose-based biochar of cassava peel for the adsorption of three cationic dyes from wastewater. Int J Biol Macromol. https://doi.org/10.1016/j.ijbiomac.2023.124534

Bhandari G, Gangola S, Dhasmana A, Rajput V, Gupta S, Malik S, Slama P (2023) Nano-biochar: recent progress, challenges, and opportunities for sustainable environmental remediation. Front Microbiol. https://doi.org/10.3389/fmicb.2023.1214870

Blaga AC, Zaharia C, Suteu D (2021) Polysaccharides as support for microbial biomass-based adsorbents with applications in removal of heavy metals and dyes. Polymers (Basel). https://doi.org/10.3390/polym13172893

Bulut Y, Aydin H (2006) A kinetics and thermodynamics study of methylene blue adsorption on wheat shells. Desalination 194:259–267. https://doi.org/10.1016/j.desal.2005.10.032

Bushra R, Mohamad S, Alias Y, Jin Y, Ahmad M (2021) Current approaches and methodologies to explore the perceptive adsorption mechanism of dyes on low-cost agricultural waste: a review. Microporous Mesoporous Mater. https://doi.org/10.1016/j.micromeso.2021.111040

Chen Q, Tan X, Liu Y, Liu S, Li M, Gu Y, Zhang P, Ye S, Yang Z, Yang Y (2020) Biomass-derived porous graphitic carbon materials for energy and environmental applications. J Mater Chem A Mater. https://doi.org/10.1039/c9ta11618d

Chen F, Sun Y, Liang C, Yang T, Mi S, Dai Y, Yu M, Yao Q (2022) Adsorption characteristics and mechanisms of Cd^{2+} from aqueous solution by biochar derived from corn stover. Sci Rep. https://doi.org/10.1038/s41598-022-22714-y

Daffalla S, Taha A et al (2024) Sustainable banana-waste-derived biosorbent for congo red removal from aqueous solutions: kinetics, equilibrium, and breakthrough studies. Water. https://doi.org/10.3390/w16101449

Das L, Sengupta S, Das P, Bhowal A, Bhattacharjee C (2021) Experimental and Numerical modeling on dye adsorption using pyrolyzed mesoporous biochar in Batch and fixed-bed column reactor: Isotherm, Thermodynamics, Mass transfer, Kinetic analysis. Surf Interf. https://doi.org/10.1016/j.surfin.2021.100985

Dawwam GE, Abdelfattah NM, Abdel-Monem MO, Jahin HS, Omer AM, Abou-Taleb KA, Mansor ES (2023) An immobilized biosorbent from *Paenibacillus dendritiformis* dead cells and polyethersulfone for the sustainable bioremediation of lead from wastewater. Sci Rep. https://doi.org/10.1038/s41598-023-27796-w

Dey AK, Dey A, Goswami R (2022) Adsorption characteristics of methyl red dye by Na_2CO_3-treated jute fibre using multi-criteria decision making approach. Appl Water Sci. https://doi.org/10.1007/s13201-022-01700-9

Ding C, Cheng W, Sun Y, Wang X (2015) Novel fungus-Fe_3O_4 bio-nanocomposites as high performance adsorbents for the removal of radionuclides. J Hazard Mater. https://doi.org/10.1016/j.jhazmat.2015.04.032

dos Reis GS, Bergna D, Grimm A, Lima EC, Hu T, Naushad M, Lassi U (2023) Preparation of highly porous nitrogen-doped biochar derived from birch tree wastes with superior dye removal performance. Colloids Surf A Physicochem Eng Asp 669:131493. https://doi.org/10.1016/j.colsurfa.2023.131493

Dutta S, Gupta B, Srivastava SK, Gupta AK (2021) Recent advances on the removal of dyes from wastewater using various adsorbents: A critical review. Mater Adv. 2, 4497–4531. https://doi.org/10.1039/d1ma00354b

Eltaweil AS, Ali Mohamed H, Abd El-Monaem EM, El-Subruiti GM (2020) Mesoporous magnetic biochar composite for enhanced adsorption of malachite green dye: characterization, adsorption kinetics, thermodynamics and isotherms. Adv Powder Technol 31:1253–1263. https://doi.org/10.1016/j.apt.2020.01.005

Fatimah I, Ramanda GD, Sagadevan S, Suratno T et al (2024) One-pot synthesis of nickel nanoparticles-embedded biochar and insight on adsorption, catalytic oxidation and photocatalytic oxidation of dye. Case Stud Chem Environ Eng. https://doi.org/10.1016/j.cscee.2024.100767

Fil BA, Ozmetin C (2012) Adsorption of cationic dye from aqueous solution by clay as an adsorbent: thermodynamic and kinetic studies, Chem Soc Pak.

Gajendiran V, Deivasigamani P, Sivamani S, Banerjee S (2024) Biochar from *Manihot esculenta* stalk as potential adsorbent for removal of reactive yellow dye. Desalination Water Treat. https://doi.org/10.1016/j.dwt.2024.100120

Gale M, Nguyen T, Moreno M, Gilliard-Abdulaziz KL (2021) Physiochemical properties of biochar and activated carbon from biomass residue: influence of process conditions to adsorbent properties. ACS Omega 6:10224–10233. https://doi.org/10.1021/acsomega.1c00530

Ghosh S, Nandasana M, Webster TJ, Thongmee S (2023) Agrowaste-generated biochar for the sustainable remediation of refractory pollutants. Front Chem. https://doi.org/10.3389/fchem.2023.1266556

Godiya CB, Martins Ruotolo LA, Cai W (2020) Functional biobased hydrogels for the removal of aqueous hazardous pollutants: Current status, challenges, and future perspectives. J Mater Chem A Mater. https://doi.org/10.1039/d0ta07028a

Gong H, Chi J, Ding Z, Zhang F, Huang J (2020) Removal of lead from two polluted soils by magnetic wheat straw biochars. Ecotoxicol Environ Saf 205:111132. https://doi.org/10.1016/j.ecoenv.2020.111132

Goswami L, Kushwaha A, Kafle SR, Kim BS (2022) Surface modification of biochar for dye removal from wastewater. Catalysts. https://doi.org/10.3390/catal12080817

Grimm A, dos Reis GS, Khokarale SG, Ekman S, Lima EC, Xiong S, Hultberg M (2023) Shiitake spent mushroom substrate as a sustainable feedstock for developing highly efficient nitrogen-doped biochars for treatment of dye-contaminated water. J Water Process Eng. https://doi.org/10.1016/j.jwpe.2023.104435

Hameed BH, Ahmad AA (2009) Batch adsorption of methylene blue from aqueous solution by garlic peel, an agricultural waste biomass. J Hazard Mater 164:870–875. https://doi.org/10.1016/j.jhazmat.2008.08.084

Hu Q, Zhang Z (2019) Application of Dubinin-Radushkevich isotherm model at the solid/solution interface: a theoretical analysis. J Mol Liq 277:646–648. https://doi.org/10.1016/j.molliq.2019.01.005

Hua Z, Pan Y, Hong Q (2023) Adsorption of Congo red dye in water by orange peel biochar modified with CTAB. RSC Adv 13:12502–12508. https://doi.org/10.1039/d3ra01444d

Ilić M, Haegel FH, Lolić A, Nedić Z, Tosti T, Ignjatović IS, Linden A, Jablonowski ND, Hartmann H (2022) Surface functional groups and degree of carbonization of selected chars from different processes and feedstock. PLoS ONE. https://doi.org/10.1371/journal.pone.0277365

Infurna G, Caruso G, Dintcheva NT (2023) Sustainable materials containing biochar particles: a review. Polymers (Basel). https://doi.org/10.3390/polym15020343

Isaeva VI, Vedenyapina MD, Kurmysheva AY, Weichgrebe D, Nair RR, Nguyen NPT, Kustov LM (2021) Modern carbon–based materials for adsorptive removal of organic and inorganic pollutants from water and wastewater. Molecules. https://doi.org/10.3390/molecules26216628

Jabar JM, Adebayo MA, Odusote YA, Yılmaz M, Rangabhashiyam S (2023) Valorization of microwave-assisted H_3PO_4-activated plantain (*Musa paradisiacal L*) leaf biochar for malachite green sequestration: models and mechanism of adsorption. Results Eng. https://doi.org/10.1016/j.rineng.2023.101129

Kim J, Bak GH, Yoo DY, Lee YI, Lee YG, Chon K (2023) Functionalization of pine sawdust biochars with Mg/Al layered double hydroxides to enhance

adsorption capacity of synthetic azo dyes: adsorption mechanisms and reusability. Heliyon. https://doi.org/10.1016/j.heliyon.2023.e14142
Kosale D, Thakur C, Singh VK (2023) Use of Jamun seed (*Syzyum cumini*) biochar for the removal of Fuchsin dye from aqueous solution. J Serb Chem Soc 88:653–667. https://doi.org/10.2298/JSC220830021K
Lei X, Hu S, Liu K, Lv X, Chen Y, Zhang Q, Jia Y, Zhong K, Wang B, Xu T (2024) Electrochemical oxidation of Rhodamine B in dye wastewater by a novel boron-doped diamond electrode: parameter optimization and degradation mechanism. Desalination Water Treat. https://doi.org/10.1016/j.dwt.2024.100243
Li X (2019) Preparation and adsorption properties of biochar/g-C_3N_4 composites for methylene blue in aqueous solution. J Nanomater. https://doi.org/10.1155/2019/2394184
Li Y, Wu Y, Chen N, Ma Y, Ji W, Sun Y (2023a) Preparation of metal oxide-loaded nickel foam adsorbents modified by biochar for the removal of cationic dyes from wastewater. Chin J Anal Chem. https://doi.org/10.1016/j.cjac.2023.100278
Li Z, Zheng Z, Li H, Xu D, Li X, Xiang L, Tu S (2023b) Review on rice husk biochar as an adsorbent for soil and water remediation. Plants. https://doi.org/10.3390/plants12071524
Liang T, Li L, Zhu C, Liu X, Li H, Su Q, Ye J, Geng B, Tian Y, Sardar MF, Huang X, Li F (2020) Adsorption of as(V) by the novel and efficient adsorbent cerium-manganese modified biochar. Water (Switzerland). https://doi.org/10.3390/w12102720
Liu M, Niu J, Zhang Z, Dou M, Wang F (2018) Potassium compound-assistant synthesis of multi-heteroatom doped ultrathin porous carbon nanosheets for high performance supercapacitors. Nano Energy 51:366–372. https://doi.org/10.1016/j.nanoen.2018.06.037
Liu J, Huang S, Wang T, Mei M, Chen S, Li J (2021) Peroxydisulfate activation by digestate-derived biochar for azo dye degradation: Mechanism and performance. Sep Purif Technol 279:119687. https://doi.org/10.1016/j.seppur.2021.119687
Mandal S, Sarkar B, Igalavithana AD, Ok YS, Yang X, Lombi E, Bolan N (2017) Mechanistic insights of 2,4-D sorption onto biochar: Influence of feedstock materials and biochar properties. Bioresour Technol 246:160–167. https://doi.org/10.1016/j.biortech.2017.07.073
Mansour RA, El Shahawy A, Attia A, Beheary MS (2020) Brilliant green dye biosorption using activated carbon derived from guava tree wood. Int J Chem Eng. https://doi.org/10.1155/2020/8053828
Melo ALFC, Carneiro MT, Morais AÍS, Viana BC, Santos FEP, Osajima JA, Bezerra RDS, Peña-Garcia RR, Almeida LC, Carrasco SM, Silva-Filho EC (2023) Using Activated Biochar from *Caryocar brasiliense Pequi* Almonds for Removing Methylene Blue Dye in an Aqueous Solution. Water (Switzerland). https://doi.org/10.3390/w15224006
Mian MM, Ao W, Deng S (2023) Sludge-based biochar adsorbent: pore tuning mechanisms, challenges, and role in carbon sequestration. Biochar. https://doi.org/10.1007/s42773-023-00288-w
Mishra A, Ojha H, Pandey J, Tiwari AK, Pathak M (2023) Adsorption characteristics of magnetized biochar derived from *Citrus limetta* peels. Heliyon. https://doi.org/10.1016/j.heliyon.2023.e20665
Monga D, Kaur P, Singh B (2022) Microbe mediated remediation of dyes, explosive waste and polyaromatic hydrocarbons, pesticides and pharmaceuticals. Curr Res Microb Sci. https://doi.org/10.1016/j.crmicr.2021.100092
Muniasamy SK, Gopala Krishna GVT, Murali V, Ravindiran G (2024) The adsorption behaviour of biochar derived from *Prosopis juliflora* with surface modified by KOH against Allura red dye. Desalination Water Treat. https://doi.org/10.1016/j.dwt.2024.100337
Muoghalu CC, Owusu PA, Lebu S, Nakagiri A, Semiyaga S, Iorhemen OT, Manga M (2023) Biochar as a novel technology for treatment of onsite domestic wastewater: a critical review. Front Environ Sci. https://doi.org/10.3389/fenvs.2023.1095920
Nath H, Saikia A, Goutam PJ, Saikia BK, Saikia N (2021) Removal of methylene blue from water using okra (*Abelmoschus esculentus* L.) mucilage modified biochar. Bioresour Technol Rep. https://doi.org/10.1016/j.biteb.2021.100689
Nnaji PC, Anadebe VC, Ezemagu IG, Onukwuli OD (2022) Potential of *Luffa cylindrica* seed as coagulation-flocculation (CF) agent for the treatment of dye wastewater: Kinetic, mass transfer, optimization and CF adsorption studies. Arab J Chem. https://doi.org/10.1016/j.arabjc.2021.103629
Ojedokun AT, Bello OS (2017) Kinetic modeling of liquid-phase adsorption of Congo red dye using guava leaf-based activated carbon. Appl Water Sci 7:1965–1977. https://doi.org/10.1007/s13201-015-0375-y
Orlando A, Franceschini F, Muscas C, Pidkova S, Bartoli M, Rovere M, Tagliaferro A (2021) A comprehensive review on Raman spectroscopy applications. Chemosensors. https://doi.org/10.3390/chemosensors9090262
Oyekanmi AA, Katibi KK, Omar RC, Ahmad A, Elbidi M, Alshammari MB, Shitu IG (2024) A novel oil palm frond magnetic biochar for the efficient adsorption of crystal violet and sunset yellow dyes from aqueous solution: synthesis, kinetics, isotherm, mechanism and reusability studies. Appl Water Sci. https://doi.org/10.1007/s13201-023-02060-8
Pandey D, Daverey A, Dutta K, Yata VK, Arunachalam K (2022) Valorization of waste pine needle biomass into biosorbents for the removal of methylene blue dye from water: kinetics, equilibrium and thermodynamics study. Environ Technol Innov. https://doi.org/10.1016/j.eti.2021.102200
Park JH, Wang JJ, Meng Y, Wei Z, DeLaune RD, Seo DC (2019) Adsorption/desorption behavior of cationic and anionic dyes by biochars prepared at normal and high pyrolysis temperatures. Colloids Surf A Physicochem Eng Asp 572:274–282. https://doi.org/10.1016/j.colsurfa.2019.04.029
Park H, Kim J, Lee YG, Chon K (2021) Enhanced adsorptive removal of dyes using mandarin peel biochars via chemical activation with NH_4Cl and $ZnCl_2$. Water (Switzerland). https://doi.org/10.3390/w13111495
Patil SR, Sutar SS, Jadhav JP (2020) Sorption of crystal violet from aqueous solution using live roots of *Eichhornia crassipes*: kinetic, isotherm, phyto and cyto-genotoxicity studies. Environ Technol Innov. https://doi.org/10.1016/j.eti.2020.100648
Pervez MN, Hassan MM, Naddeo V (2024) Separation of cationic methylene blue dye from its aqueous solution by S-sulfonated wool keratin-based sustainable electrospun nanofibrous membrane biosorbent. Sep Purif Technol. https://doi.org/10.1016/j.seppur.2023.125903
Phuong DTM, Loc NX, Miyanishi T (2019) Efficiency of dye adsorption by biochars produced from residues of two rice varieties, Japanese *Koshihikari* and *Vietnamese IR50404*. Desalination Water Treat 165:333–351. https://doi.org/10.5004/dwt.2019.24496
Pinky NS, Bin Mobarak M, Mustafi S, Zesanur Rahman M, Nahar A, Saha T, Mohammed Bahadur N (2023) Facile preparation of micro-porous biochar from Bangladeshi sprouted agricultural waste (corncob) via in-house built heating chamber for cationic dye removal. Arab J Chem 16:105080. https://doi.org/10.1016/j.arabjc.2023.105080
Praveen S, Jegan J, Bhagavathi Pushpa T, Gokulan R, Bulgariu L (2022) Biochar for removal of dyes in contaminated water: an overview. Biochar. https://doi.org/10.1007/s42773-022-00131-8
Ramath R, Sukumaran AM, Ramachandran A, Basheer SB (2023) Methyl orange dye adsorption and degradation at low temperature using iron oxide-incorporated biochar derived from industrial by-products. Bioresour Technol Rep. https://doi.org/10.1016/j.biteb.2023.101470
Ray A (2020) Characterization of biochars from various agricultural by-products using FTIR spectroscopy, SEM focused with image processing. Int J Agric Environ Biotechnol. https://doi.org/10.30954/0974-1712.04.2020.6
Saghir S, Pu C, Fu E, Wang Y, Xiao Z (2022) Synthesis of high surface area porous biochar obtained from pistachio shells for the efficient adsorption of organic dyes from polluted water. Surf Interf 34:102357. https://doi.org/10.1016/j.surfin.2022.102357
Sahu S, Pahi S, Tripathy S, Singh SK, Behera A, Sahu UK, Patel RK (2020) Adsorption of methylene blue on chemically modified lychee seed biochar: dynamic, equilibrium, and thermodynamic study. J Mol Liq. https://doi.org/10.1016/j.molliq.2020.113743
Salah omer AA et al (2022) Adsorption of crystal violet and methylene blue dyes using a cellulose-based adsorbent from sugercane bagasse: characterization, kinetic and isotherm studies. J Market Res 19:3241–3254. https://doi.org/10.1016/j.jmrt.2022.06.045
Sangsuk S, Napanya P, Tasen S, Baiya P, Buathong C, Keeratisoontornwat K, Suebsiri S (2023) Production of non-activated biochar based on *Biden pilosa* and its application in removing methylene blue from aqueous solutions. Heliyon 9:e15766. https://doi.org/10.1016/j.heliyon.2023.e15766
Santhosh C, Daneshvar E, Tripathi KM, Baltrėnas P, Kim TY, Baltrėnaitė E, Bhatnagar A (2020) Synthesis and characterization of magnetic biochar adsorbents for the removal of Cr(VI) and Acid orange 7 dye from aqueous solution. Environ Sci Pollut Res 27:32874–32887. https://doi.org/10.1007/s11356-020-09275-1

Satyam S, Patra S (2024) Innovations and challenges in adsorption-based wastewater remediation: a comprehensive review. Heliyon. https://doi.org/10.1016/j.heliyon.2024.e29573

Shan D, Shao Z, Liu X, Wang Y, Liu Y, Dai Y (2022) Efficient adsorption of three dyes by soybean residue (okara) biochar in an aqueous solution. Desalination Water Treat 266:212–225. https://doi.org/10.5004/dwt.2022.28653

Singh M, Ahsan M, Pandey V, Singh A, Mishra D, Tiwari N, Singh P, Karak T, Khare P (2022) Comparative assessment for removal of anionic dye from water by different waste-derived biochar vis a vis reusability of generated sludge. Biochar. https://doi.org/10.1007/s42773-022-00140-7

Srivatsav P, Bhargav BS, Shanmugasundaram V, Arun J, Gopinath KP, Bhatnagar A (2020) Biochar as an eco-friendly and economical adsorbent for the removal of colorants (Dyes) from aqueous environment: a review. Water (Switzerland). https://doi.org/10.3390/w12123561

Sterenzon E, Vadivel VK, Gerchman Y, Luxbacher T, Narayanan R, Mamane H (2022) Effective removal of acid dye in synthetic and silk dyeing effluent: isotherm and kinetic studies. ACS Omega 7:118–128. https://doi.org/10.1021/acsomega.1c04111

Subratti A, Vidal JL, Lalgee LJ, Kerton FM, Jalsa NK (2021) Preparation and characterization of biochar derived from the fruit seed of *Cedrela odorata L* and evaluation of its adsorption capacity with methylene blue. Sustain Chem Pharm. https://doi.org/10.1016/j.scp.2021.100421

Sun L, Chen D, Wan S, Yu Z (2015) Performance, kinetics, and equilibrium of methylene blue adsorption on biochar derived from eucalyptus saw dust modified with citric, tartaric, and acetic acids. Bioresour Technol 198:300–308. https://doi.org/10.1016/j.biortech.2015.09.026

Sutar S, Patil P, Jadhav J (2022) Recent advances in biochar technology for textile dyes wastewater remediation: a review. Environ Res 209:112841. https://doi.org/10.1016/j.envres.2022.112841

Tcheka C, Conradie MM, Assinale VA, Conradie J (2024) Mesoporous biochar derived from Egyptian doum palm (*Hyphaene thebaica*) shells as low-cost and biodegradable adsorbent for the removal of methyl orange dye: Characterization, kinetic and adsorption mechanism. Chem Phys Impact. https://doi.org/10.1016/j.chphi.2023.100446

Tharayil J, Chinnaiyan P (2023) Sustainable waste valorisation: novel *Areca catechu* L. husk biochar for anthraquinone dye adsorption—characterization, modelling, kinetics, and isotherm studies. Results Eng. https://doi.org/10.1016/j.rineng.2023.101624

Tokarčíková M, Peikertová P, Čech Barabaszová K, Životský O, Gabor R, Seidlerová J (2023) Regeneration possibilities and application of magnetically modified biochar for heavy metals elimination in real conditions. Water Resour Ind. https://doi.org/10.1016/j.wri.2023.100219

Tomin O, Vahala R, Yazdani MR (2024) Synthesis and efficiency comparison of reed straw-based biochar as a mesoporous adsorbent for ionic dyes removal. Heliyon. https://doi.org/10.1016/j.heliyon.2024.e24722

Tulashie SK, Kotoka F, Botchway BN, Adu K (2022) Removal of reactive violet 5 azo dye (V5R) using bamboo, and calabash biochar. Heliyon. https://doi.org/10.1016/j.heliyon.2022.e10908

Üner O, Geçgel Ü, Bayrak Y (2016) Adsorption of methylene blue by an efficient activated carbon prepared from *Citrullus lanatus* rind: kinetic, isotherm, thermodynamic, and mechanism analysis. Water Air Soil Pollut. https://doi.org/10.1007/s11270-016-2949-1

Velić N, Stjepanović M, Pavlović S, Bagherifam S, Banković P, Jović-Jovičić N (2023) Modified lignocellulosic waste for the amelioration of water quality: adsorptive removal of congo red and nitrate using modified poplar sawdust. Water (Switzerland). https://doi.org/10.3390/w15213776

Viotti P, Marzeddu S, Antonucci A, Décima MA, Lovascio P, Tatti F, Boni MR (2024) Biochar as alternative material for heavy metal adsorption from groundwaters: lab-scale (Column) experiment review. Materials. https://doi.org/10.3390/ma17040809

Wang C, Wang X, Li N, Tao J, Yan B, Cui X, Chen G (2022) Adsorption of lead from aqueous solution by biochar: a review. Clean Technologies. https://doi.org/10.3390/cleantechnol4030039

Wang Y, Luo J, Qin J, Huang Y, Ke T, Luo Y, Yang M (2023) Efficient removal of phytochrome using rice straw-derived biochar: adsorption performance, mechanisms, and practical applications. Bioresour Technol. https://doi.org/10.1016/j.biortech.2023.128918

Wang Y, Chen L, Zhu Y, Fang W, Tan Y, He Z, Liao H (2024) Research status, trends, and mechanisms of biochar adsorption for wastewater treatment: a scientometric review. Environ Sci Eur. https://doi.org/10.1186/s12302-024-00859-z

Wei F, Zhu Y, He T, Zhu S, Wang T, Yao C, Yu C, Huang P, Li Y, Zhao Q, Song W (2022) Insights into the pH-dependent adsorption behavior of ionic dyes on phosphoric acid-activated biochar. ACS Omega 7:46288–46302. https://doi.org/10.1021/acsomega.2c04799

Yang X, Zhu W, Song Y, Zhuang H, Tang H (2021) Removal of cationic dye BR46 by biochar prepared from *Chrysanthemum morifolium* Ramat straw: a study on adsorption equilibrium, kinetics and isotherm. J Mol Liq 340:116617. https://doi.org/10.1016/j.molliq.2021.116617

Yao X, Ji L, Guo J, Ge S, Lu W, Chen Y, Cai L, Wang Y, Song W (2020) An abundant porous biochar material derived from wakame (*Undaria pinnatifida*) with high adsorption performance for three organic dyes. Bioresour Technol 318:124082. https://doi.org/10.1016/j.biortech.2020.124082

Yazdani MR, Tuutijärvi T, Bhatnagar A, Vahala R (2016) Adsorptive removal of arsenic(V) from aqueous phase by feldspars: kinetics, mechanism, and thermodynamic aspects of adsorption. J Mol Liq 214:149–156. https://doi.org/10.1016/j.molliq.2015.12.002

Yazdani MR, Duimovich N, Tiraferri A, Laurell P, Borghei M, Zimmerman JB, Vahala R (2019) Tailored mesoporous biochar sorbents from pinecone biomass for the adsorption of natural organic matter from lake water. J Mol Liq. https://doi.org/10.1016/j.molliq.2019.111248

Zand AD, Abyaneh MR (2020) Adsorption of Lead, manganese, and copper onto biochar in landfill leachate: implication of non-linear regression analysis. Sustain Environ Res. https://doi.org/10.1186/s42834-020-00061-9

Zeng H, Qi W, Zhai L, Wang F, Zhang J, Li D (2021) Magnetic biochar synthesized with waterworks sludge and sewage sludge and its potential for methylene blue removal. J Environ Chem Eng 9:105951. https://doi.org/10.1016/j.jece.2021.105951

Zhang N, Reguyal F, Praneeth S, Sarmah AK (2023) A green approach of biochar-supported magnetic nanocomposites from white tea waste: production, characterization and plausible synthesis mechanisms. Sci Total Environ 886:163923. https://doi.org/10.1016/j.scitotenv.2023.163923